

Simulating Cardiac Fluid Dynamics in the Human Heart

Marshall Davey^{1,*}, Charles Puelz^{2,*}, Simone Rossi³, Margaret Anne Smith³, David R. Wells³, Greg Sturgeon⁴,
W. Paul Segars⁴, John P. Vavalle⁵, Charles S. Peskin⁶, and Boyce E. Griffith⁷⁻¹⁰

¹Curriculum in Bioinformatics and Computational Biology, University of North Carolina, Chapel Hill, NC, USA

²Department of Pediatrics-Cardiology, Baylor College of Medicine and Texas Children's Hospital, Houston, TX, USA

³Department of Mathematics, University North Carolina, Chapel Hill, NC, USA

⁴Department of Radiology, Duke University Medical Center, Durham, NC, USA

⁵Division of Cardiology, Department of Medicine, University of North Carolina School of Medicine, Chapel Hill, NC, USA

⁶Courant Institute of Mathematical Sciences, New York University, New York, NY, USA

⁷Departments of Mathematics and Biomedical Engineering, University of North Carolina, Chapel Hill, NC, USA

⁸Carolina Center for Interdisciplinary Applied Mathematics, University of North Carolina, Chapel Hill, NC, USA

⁹Computational Medicine Program, University of North Carolina School of Medicine, Chapel Hill, NC, USA

¹⁰McAllister Heart Institute, University of North Carolina School of Medicine, Chapel Hill, NC, USA

*These authors contributed equally to this work

July 7, 2023

Abstract

Cardiac fluid dynamics fundamentally involves interactions between complex blood flows and the structural deformations of the muscular heart walls and the thin, flexible valve leaflets. There has been longstanding scientific, engineering, and medical interest in creating mathematical models of the heart that capture, explain, and predict these fluid-structure interactions. However, existing models that account for interactions among the blood, the actively contracting myocardium, and the cardiac valves are limited in their abilities to predict valve performance, resolve fine-scale flow features, or use realistic descriptions of tissue biomechanics. Here we introduce and benchmark a comprehensive mathematical model of cardiac fluid dynamics in the human heart. Our model accounts for all major cardiac structures and is calibrated using tensile tests of human tissue specimens to reflect the influences of myocyte and collagen fiber alignment. It includes biomechanically detailed three-dimensional descriptions of all four cardiac valves, including the chordae tendineae and papillary muscles. We demonstrate that the model generates physiologic dynamics, including realistic pressure-volume loops that automatically capture isovolumetric contraction and relaxation, and predicts fine-scale flow features. Critically, none of these outputs are prescribed; instead, they emerge from interactions within the integrative model. Such models can serve as tools for predicting the impacts of medical devices or clinical interventions, particularly those that fundamentally involve the heart valves. They also can serve as platforms for mechanistic studies of cardiac pathophysiology and dysfunction, including congenital defects, cardiomyopathies, and heart failure, that are difficult or impossible to perform in patients.

Keywords: Fluid-structure interaction; cardiac modeling; heart valves; immersed boundary method.

Introduction

The heart is the most dynamic organ in the body and has been a focus of scientific and medical inquiry for millennia. Studies of the human heart began with detailed descriptions of its gross anatomy and have evolved to encompass a diverse set of research questions and approaches.¹ Current studies vary widely in both methodology and scale, from wet-lab experiments of cell function to analytic characterization of muscle fiber orientation.^{2,3} Animal models were

some of the first systems used to understand the heart as a dynamic system *in vivo*,^{4,5} but they are limited by the invasive nature of the experimental measurements, which impact the observed dynamics, as well as by the differences in anatomy and physiology of other animals as compared to humans. Imaging and catheterization studies provide a means to study human cardiac function *in vivo*, but although technological advancements continue to improve these approaches, they can be costly, are limited in the detail of their measurements, and can pose risks to human subjects. Further, whereas methods for measuring cardiac function can assess the present state of the heart, models are critical for predicting future states of the heart following growth, remodeling, or clinical intervention.

Predictive mathematical models of the heart can capture important features of cardiac function and serve as platforms for treatment planning and medical device design.⁶ Despite substantial scientific, engineering, and medical research, however, previous computer models of the heart that account for interactions among the blood, the actively contracting myocardium, and the cardiac valves have included important simplifications that impact their ability to predict valve performance, resolve fine-scale flow features, or use realistic models of tissue biomechanics. To our knowledge, the earliest four-chambered heart model was developed by Peskin and McQueen^{7,8} using the immersed boundary method.⁹ Although their model captured the complex interactions of the heart muscle, valves, and blood, the anatomic structures were comprised of systems of one-dimensional elastic fibers that are challenging to calibrate to human data. Baillargeon et al.¹⁰ constructed a model that included detailed descriptions of the myocardium coupled to an electrophysiology model for the four heart chambers. However, to obtain boundary conditions for the chamber walls, they used a simplified fluid model that neglected spatial variations in the pressure and velocity fields. Fedele et al.¹¹ created a biomechanically detailed four-chambered electromechanical heart model coupled to a zero-dimensional blood circulation model via pressure boundary conditions. Their model produced pressure-volume loops in the atria and ventricles in good agreement with clinical data but also did not capture fine-scale flow features in the chambers and around valve leaflets because of its simplified treatment of the intracardiac fluid mechanics. Kariya et al.¹² built a four-chambered heart model based on the arbitrary Lagrangian-Eulerian method. Their construction included models for oxygen transport, electrophysiology, and the valve leaflets. However, their approach used a simplified biomechanics model that neglects nonlinear and anisotropic responses of real heart valves and required the explicit modeling of contact between structures.

Here we introduce and benchmark a new comprehensive fluid-structure interaction (FSI) model of the human heart. The model anatomy is derived from cardiac computed tomography (CT) imaging and includes fully three-dimensional descriptions of all major cardiac structures, including the atria, ventricles, mitral and tricuspid valves and their chordae tendineae and papillary muscles, aortic and pulmonary valves, and great vessels. The biomechanical models of the heart and its valves are parameterized using experimental tensile test data obtained exclusively from human tissue specimens.¹³⁻¹⁷ Model-based approaches¹⁸⁻²⁰ consistent with earlier experimental work²¹⁻²⁶ describe the heart's fiber architecture. FSI simulations use the immersed finite element/finite difference (IFED) version²⁷ of the immersed boundary method,⁹ which automatically handles contact between structures, including the valve leaflets. Several recent methodological developments enabled this model, including modern tetrahedral mesh generation techniques²⁸ and stabilized nodal IFED methods.²⁹ Our model generates physiological stroke volumes, pressure-volume loops, and valvular pressure-flow relationships, illustrating its potential for predicting cardiac function in both health and disease.

Results

Modeling Human Cardiac Anatomy and Physiology

The defining feature of the present model is that all of its dynamics emerge from interactions among its components. We prescribe only the anatomy and physiology, including tissue properties, muscle activation timings, and physiological boundary conditions. Fig. 1 provides an overview of the model and Fig. S1 shows the finite element mesh used in our simulations.

The anatomy of the heart chambers and the nearby great vessels were reconstructed from deidentified cardiac CT images of a healthy adult male provided by Siemens Healthineers. The images used to reconstruct the model correspond to the early diastolic phase of the cardiac cycle, when the heart is in its most relaxed state.³⁰ It can be

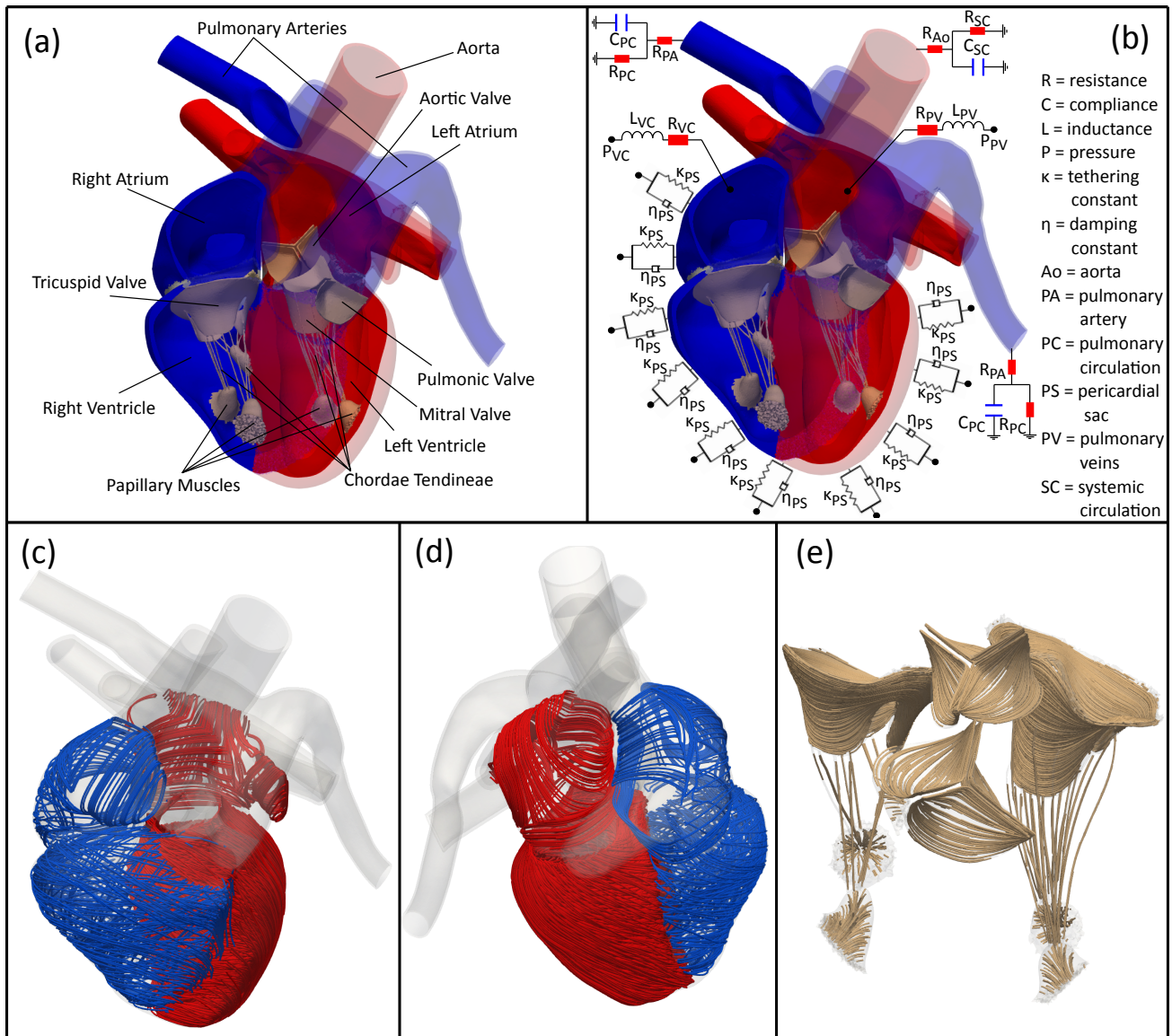


Figure 1: Anatomical and physiological aspects of the heart model. Panel (a) visualizes the structural components of the heart model. The anterior portions of the chambers and great vessels are transparent to reveal the four valves and valvular complexes. Panel (b) provides a schematic of the reduced order models used for the pericardial sac, the systemic and pulmonary circulations, and the venous return to the atria. Panels (c) and (d) depict the main myocardial fibers from two different views with the right heart and left heart chambers depicted in blue and red, respectively, and panel (e) visualizes the main fiber directions on the valve leaflets, chordae, and papillary muscles. The fiber coloration was chosen for visual clarity.

difficult or impossible to capture the valve leaflets and chordae tendineae from whole-heart CT images,³¹ and, indeed, the images used in this construction do not clearly show these structures. Consequently, we generated idealized anatomical models of the valve leaflets based on dimensions obtained from studies of human valves and merged these with the CT-derived chamber anatomy.

Cardiac tissues are highly anisotropic. In the myocardium, this a consequence of the alignment and organization of the muscle fibers.³² Likewise, the mechanical behavior of the valve leaflets is characterized by families of aligned collagen fibers.¹⁶ To capture these histological features within the modeled anatomy, we created a local coordinate system in each mesh element that is aligned with the principal or mean direction of anisotropy, such as the experimentally characterized relationships between fiber angle and transmural position within the ventricular myocardium.²⁶ The

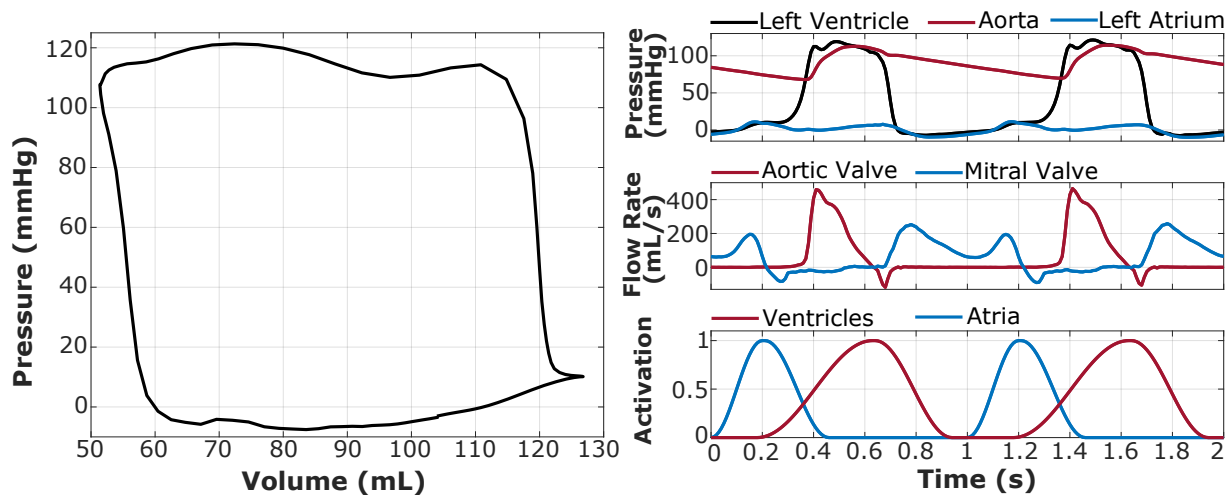


Figure 2: The left ventricular pressure-volume loop shown in the left panel captures characteristics of the cardiac cycle, including the isovolumetric phases and the stroke volume. The right panels show pressure, flow rate, and activation waveforms for two successive cardiac cycles. The pressure-volume loop corresponds to the second cycle shown, which is cycle five from our simulation results.

mechanical responses of all structural components are defined by hyperelastic energy functionals, and the contractile mechanics of the myocardium are modeled by an active strain approach.³³ Different strain-energy functionals are used for different structures to reflect their specific material properties, and different activation waveforms are specified for the atria and the ventricles. Supplementary Information Section *Left Ventricular End-Diastolic Pressure-Volume Relationship* briefly discusses validation of the passive response of our left ventricle model using the methodology of Klotz et al.;³⁴ see Fig. S2.

The pericardium constrains the motion of the ventricular wall, and accounting for these constraints is critical to achieve proper contraction and ventricular wall thickening during systole.³⁵ As in earlier work,³⁵ the effect of the pericardium on myocardial movement is modeled by a parallel spring and dashpot boundary condition applied in the normal direction along the deformed epicardium.

At the length scale of the heart, blood behaves like a Newtonian fluid,⁷ and the dynamics of blood are well approximated by the incompressible Navier-Stokes equations. Afterload provided by the systemic and pulmonary circulations are described using three-element Windkessel models³⁶ applied at locations where the ascending aorta and the left and right pulmonary artery branches intersect the boundary of the computational domain. Venous return is modeled by pressure-driven flow sources located in each atrium.³⁷

Calibration was primarily accomplished, as described in Methods Section *Blood and Circulation*, by tuning the Windkessel model parameters to the outflow generated by contraction of the left ventricle via a process that mimics the baroreceptor reflex, which is a physiological control mechanism that adjusts vascular tone to maintain physiological blood pressure.³⁸ We also adjusted the timing and magnitude of the atrial and ventricular contractions. We emphasize, however, that many of these measures vary widely across the adult population,³⁹ and obtaining these statistics from both patients and healthy subjects often relies on indirect estimation (e.g., determining left ventricular volume as the volume of an ellipsoid with long axis and short axis measurements obtained via echocardiography). Because of the high variability of these performance statistics across the adult population, it is important to ensure that our model captures intrinsic features of the cardiac cycle that cannot be summarized by simple statistics, such as the isovolumetric phases and the outflow and atrioventricular valve flow rate waveforms.

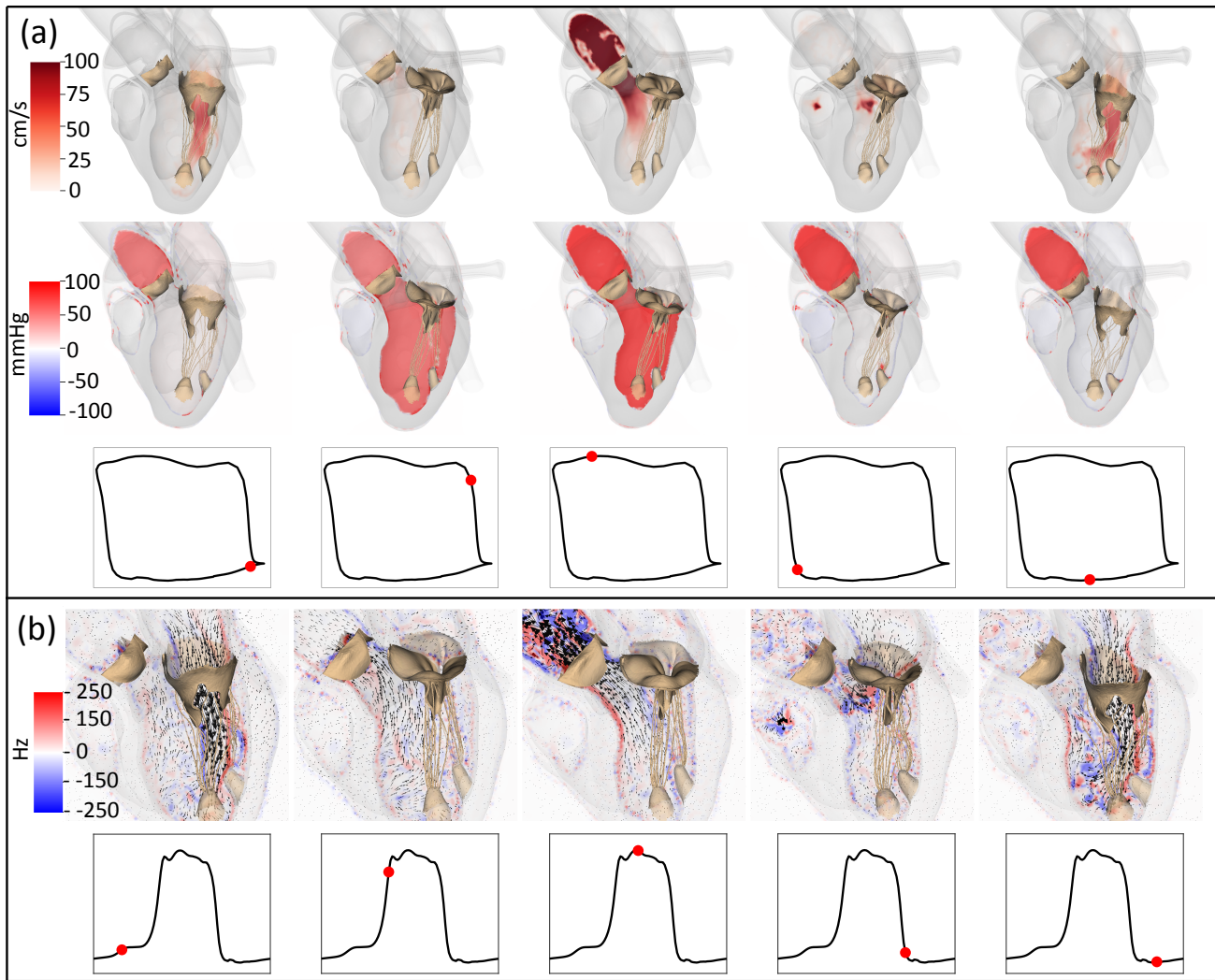


Figure 3: Cardiac fluid dynamics. (a) Top and middle panels show renderings of blood velocity magnitude and pressure, respectively, along a plane bisecting the aortic and mitral valves with semi-transparent renderings of the chambers at five timepoints in the cardiac cycle. The bottom panels show the pressure-volume loop along with a red marker indicating the point in the cardiac cycle that is being visualized in the top and middle rows. (b) Top panel shows renderings of blood velocity vectors along a plane bisecting the aortic and mitral valves with semi-transparent renderings of the chambers as well as the component of vorticity normal to the bisecting plane at five timepoints in the cardiac cycle. The left ventricular pressure waveform is included beneath, and the red marker corresponds to the point in the cardiac cycle that is being visualized in the top row.

	EDV (mL)	ESV (mL)	SV (mL)	EF	CO (L·min ⁻¹)
Model	127.58	52.0	75.58	0.59	4.5
Reference ³⁸	120	50	70	0.58	4.2

Table 1: Variables extracted from the pressure-volume loop data. ESV = end systolic volume, EDV = end diastolic volume, SV = stroke volume, EF = ejection fraction, and CO = cardiac output. CO is directly computed from the stroke volume and the heart rate (60 BPM). Clinically, CO is commonly determined from oxygen saturation measurements during cardiac catheterization or estimated using Doppler echocardiography.³⁹

Cardiac Fluid Dynamics

Contraction in the heart model is driven using time-periodic atrial and ventricular activation waveforms at a heart rate of 60 beats per minute (BPM). The model reaches an approximate periodic steady state after five cycles. The results

presented here focus on left ventricular dynamics because of the large body of available clinical and experimental data. The left ventricular pressure-volume relation, shown in Fig. 2, characterizes left-ventricular performance. The left panel shows the mean pressure sampled within the left ventricle plotted against the left ventricular volume to generate a pressure-volume loop. The right panels of Fig. 2 depict pressure waveforms measured from the left atrium, left ventricle, and aorta as well as flow rate waveforms measured through the aortic and mitral valves. Fig. S3 shows left ventricular volume data used to generate the pressure-volume relation. Pressure-volume loop data are used to calculate end-systolic volume, end-diastolic volume, stroke volume, ejection fraction, and cardiac output, which are summarized in Table 1. Reference values for a healthy adult are included for comparison.

Fig. 3(a) shows the blood velocity magnitude and pressure on a plane through the left atrium, left ventricle, and part of the ascending aorta that approximately bisects the aortic and mitral valves. These quantities are shown along with translucent renderings of the myocardium and fully opaque renderings of the aortic valve and the mitral valve apparatus. Each of the five columns corresponds to a timepoint in the cardiac cycle, including isovolumetric contraction (second column) and relaxation (fourth column). The red markers in the pressure-volume curves in the bottom row correspond to the same time points as the pressure and volume data in the top and middle rows for reference. Fig. 3(b) depicts the vorticity and velocity vector field on a slice through the left heart with a time series plot of left-ventricular pressure included beneath for reference. Periods of isovolumetric contraction and relaxation are clearly seen in the second and fourth columns, respectively.

Cardiac Valve Dynamics

Fully three-dimensional and biomechanically detailed descriptions of the cardiac valves are key characteristics of the model. Fig. 4 provides visualizations of the deformations of the aortic and mitral valves along with flow rate waveforms measured within the valve annuli. Both valves are shown from top and side views to highlight the opening and closing dynamics of the leaflets. The side view of the mitral valve includes the chordae and papillary muscles to highlight their role in maintaining closure of the valve during peak ventricular systole.

Discussion

The pressure-volume relationship identifies important quantitative and qualitative features of the cardiac cycle. These include the isovolumetric periods during contraction and relaxation, when pressure is respectively increasing and decreasing in the left ventricle, but neither the aortic valve nor the mitral valve are permitting flow. We obtain pressure-volume relationships that do not perfectly mirror pressure-volume curves seen in medical textbooks³⁸ or simulations using ideal (diode-like) valve models,⁴⁰ but that nonetheless are similar to clinical measurements appearing in the literature.^{41,42} One clear feature in the pressure-volume relation generated by the model that would not be captured by a model with ideal valves is the cusp in the bottom-right of the curve, which corresponds to the mitral valve closing transient. In vivo recordings show similar volume losses during ‘isovolumetric’ contraction;^{41,42} see Figs. S4 and S5(a). These volume losses, however, are accompanied by a larger gain in left ventricular pressure compared to the model, highlighted in Fig. S5(a), resulting in a notable lack of a sharp cusp in the in vivo examples. In contrast to the sharp cusp in the pressure-volume relationship generated by the mitral valve closing transient, the volume change resulting from the aortic valve transient occurs with a larger change in left ventricular pressure. This is in good agreement with clinical aortic flow data obtained from healthy subjects⁴³ (see Fig. S5(b)).

The aortic valve closure transient seen in column 4 of Fig. 4(a) yields a small (4.01 mL) regurgitant flow volume and is in excellent qualitative agreement with human clinical data,⁴³ as detailed in Fig. S5(b). The mitral flow rate waveform can be quantitatively assessed using the measured deceleration time and the ratio of the peak magnitudes of the so-called E and A flow rate waveforms, which for our model are respectively 250 ms and 1.35. These values fall within the expected ranges for healthy adults.⁴⁴ We remark, however, that clinical measurements typically use blood velocity waveforms obtained via Doppler echocardiography. Obtaining comparable measurements from the model would require simulating the acquisition protocols used clinically. The mitral valve flow rate waveform also captures

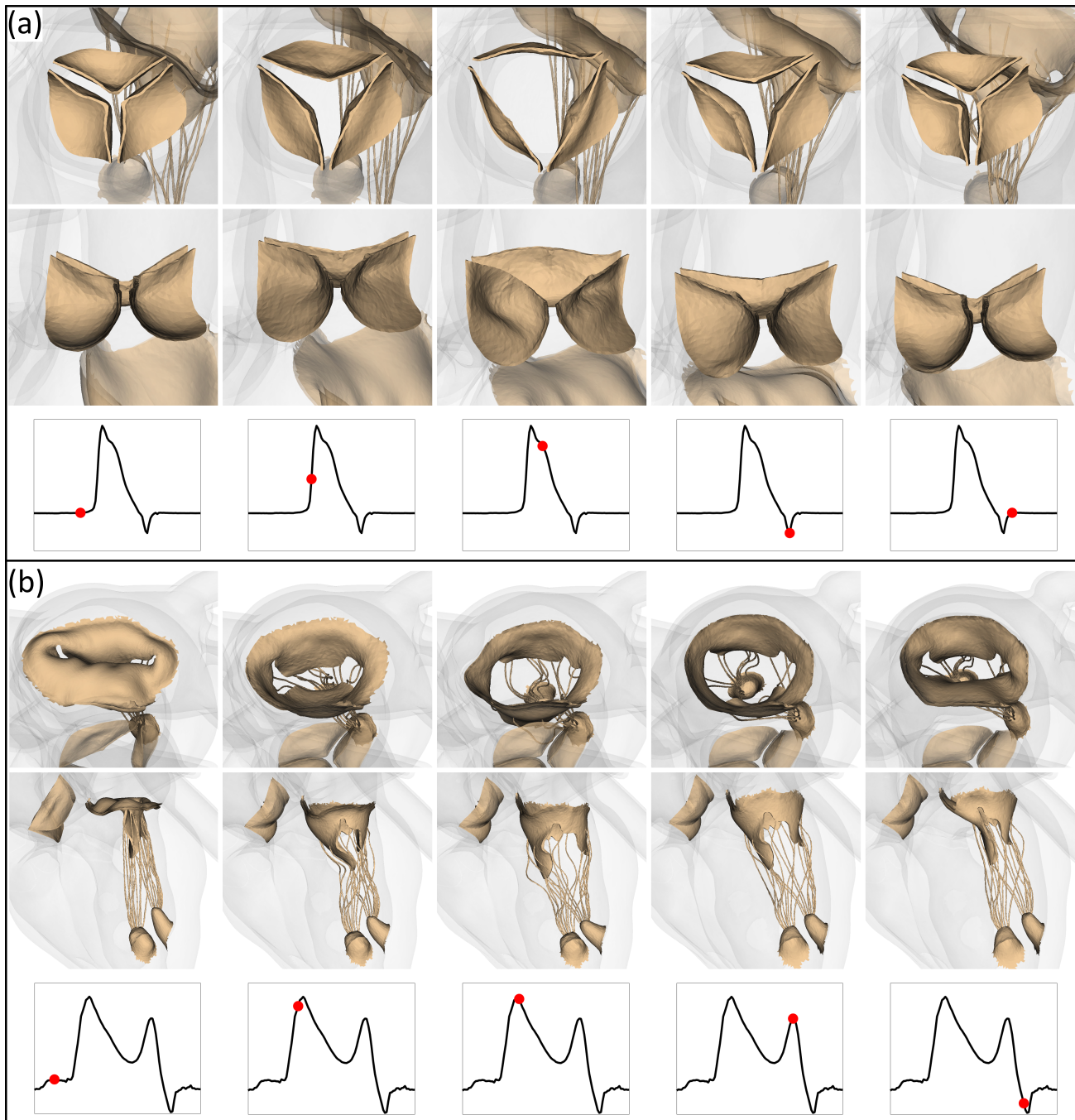


Figure 4: Cardiac valve dynamics. (a) The top panels show the aortic valve deformations from two different views for five time points in the cardiac cycle. The bottom panels depict the aortic flow rate waveform along with a red marker corresponding to the same timepoint visualized in the cardiac cycle. (b) The top panels show the mitral valve deformations from two different views for five time points throughout a cardiac cycle. The bottom set of panels depict the mitral flow rate waveform along with a red marker corresponding to the same timepoint visualized in the cardiac cycle.

many complex qualitative features of in vivo canine studies of mitral valve flow rates.⁴⁵ This includes a mitral valve closing transient during early ventricular contraction before the valve closes completely, highlighted in the fifth column of Fig. 4(b). During this period in our model, a small (5.27 mL) regurgitant flow volume is lost from the left ventricle into the left atrium. This behavior has been clearly seen in canine experimental studies, and Fig. S5(a) provides a

direct comparison between our model and such experimental data.

Overall, because the dynamics of our heart model all result from mechanistic interactions among the structures of the heart and the blood, the level of agreement with existing clinical and experimental data is excellent. Indeed, a strength of the model is that it captures the subtleties of in vivo pressure-flow relations, such as the closing transients and resultant volume changes, rather than emulating ideal pressure-volume curves that are achieved by non-compliant diode-like descriptions of the valves. Further, a major advantage of our model is its ability to directly and simultaneously access metrics such as flows through the valve annuli and localized pressures. Such data are critical for, e.g., simulation studies of treatments for structural heart disorders such as mitral valve regurgitation. The discussion of translational applications for this model is centered on valvular disorders because, unlike other whole-heart models, this model has three-dimensional descriptions of the valves with material properties that reflect human valvular tissue. Indeed, valvular heart diseases represent a substantial and rapidly growing burden on public health throughout the world.⁴⁶ These include rheumatic heart disease, which primarily affects young people between the ages of 5 and 15 and causes permanent damage to one or more heart valves, along with aortic stenosis and mitral regurgitation, which are mainly diseases of the elderly. This model is also relevant for mechanistic studies of cardiac dysfunction, such as reduced ventricular compliance from cardiomyopathy and discordant or non-extant contraction following acute myocardial infarction, and congenital heart defects, such as those within the spectrum of single ventricle physiology. In these cases, our framework could lead to detailed insights into experimental treatments and surgeries that can be used to improve clinical care and corresponding outcomes.

Materials and Methods

Anatomical Model

The anatomy of the heart chambers and the nearby great vessels were reconstructed from cardiac CT images (voxel size 0.32 mm×0.32 mm×0.4 mm) of a healthy adult male provided by Siemens Healthineers. These images were fully deidentified, and the study team has no way to determine the identity of the subject. Chamber reconstruction used methods previously detailed by Segars et al.^{47,48} Because the cardiac valves were obscured in the CT images, we generated idealized anatomical models of the valves with dimensions that are consistent with prior experimental studies of human heart valves. The aortic valve leaflet geometry¹⁸ reflects the sinus height,⁴⁹ valve diameter,⁵⁰ lunulae coaptation height,⁵⁰ and leaflet thickness⁵¹ of human aortic valves. The pulmonary valve leaflets are a replica of the aortic valve leaflets that were scaled to fit within the model pulmonary artery. The mitral valve leaflet surface geometry was built using a set of parametric equations derived from mitral valve imaging data,⁵² which was further modified to match the thickness⁵³ and length⁵⁴ of human mitral valves. The tricuspid valve leaflet geometry was based on valve dissection studies^{55,56} and has three identical leaflets that were adjusted for length to ensure complete closure during systole. The papillary muscles were placed in locations identified in the CT images and connected to the atrioventricular valves by chordae tendineae. Marginal chordae were uniformly distributed along the mitral and tricuspid valve leaflet edges, and strut and basal chordae were added to the mitral valve leaflets to prevent prolapse.⁵⁷ These valve models were subsequently merged with the CT-derived chamber anatomy, yielding the model illustrated in Fig. 1(a).

We used TetWild²⁸ to construct a monolithic, conforming tetrahedral mesh that includes the myocardium, valves, cardiac skeleton, and great vessels. The mesh used by our model contains approximately 2.4M elements with an average diameter of 1.17 mm. The mesh is partitioned into subdomains, which are groups of elements that share the same constitutive model and material properties. Subdomains defined in the model include: the left and right atria; the left and right ventricles; the aortic and pulmonary valves; the mitral and tricuspid valves, including the valve cusps, chordae tendinae, and papillary muscles; the cardiac skeleton; and short segments of the great vessels, including the ascending aorta, pulmonary artery, superior and inferior vena cavae, and pulmonary veins. Because these structures are all described within a single conforming mesh, no additional mechanical coupling conditions need to be imposed along interfaces between subdomains. The anatomy captured in the model fits within a bounding box with dimensions 20 cm×11.6 cm×17.4 cm, with the longest dimension corresponding to the distance between the branch termini of the

pulmonary artery. Fig. S1 shows two perspectives of the heart mesh and selected subdomains, with a focus on the left ventricle and mitral valve apparatus.

Cardiac Biomechanics Models

Fiber architecture

To describe the local material coordinate directions that determine the tissue anisotropy, we created an orthonormal reference frame $\{\mathbf{e}_f, \mathbf{e}_s, \mathbf{e}_n\}$ in each element of the structural mesh. Briefly, in the myocardium, \mathbf{e}_f is the principal myofiber orientation, \mathbf{e}_s points in the transmural direction (from the endocardium to the epicardium), and $\mathbf{e}_n = \mathbf{e}_f \times \mathbf{e}_s$. The material axes in the valve leaflets capture the collagen fiber architecture identified in human heart valves.^{22,23} The \mathbf{e}_f direction field describes the mean collagen fiber orientation and runs from commissure to commissure in each valve, and \mathbf{e}_s runs radially from the valve ring, where the leaflet intersects the myocardium, to the free edge. To account for fiber angle dispersion within the valve leaflets, our valve biomechanics models use two distinguished collagen fiber directions, $\mathbf{e}_{f\pm} = \cos(\theta_f)\mathbf{e}_f \pm \sin(\theta_f)\mathbf{e}_s$. These directions are rotations of \mathbf{e}_f about $\mathbf{e}_n = \mathbf{e}_f \times \mathbf{e}_s$ by the angle $\pm\theta_f$, which is a material parameter fit to experimental data. In the chordae tendineae, \mathbf{e}_f is aligned with the long axis of each chord. Fig. 1(c–d) visualize the myocardial fiber directions, and Fig. 1(e) shows the valve leaflets' mean collagen fiber direction with the fibers for the chordae and papillary muscles.

We use a harmonic interpolation technique that has been widely adopted in model-based approaches to describe cardiac fiber architecture.⁵⁸ Specifically, on each subdomain of the structure's reference configuration Ω_0^s , we construct functions $\phi(\mathbf{X})$ that satisfy $\nabla^2\phi(\mathbf{X}) = 0$, with $\mathbf{X} \in \Omega_0^s$, and we use each resulting function to determine a local coordinate direction via $\nabla\phi(\mathbf{X})/\|\nabla\phi(\mathbf{X})\|$. The orientation of each direction field is controlled through boundary conditions for $\phi(\mathbf{X})$ that are imposed along the subdomain boundaries. For instance, to model a group of fibers that originates on one part of the subdomain boundary and terminates along another part of the boundary, we respectively impose the Dirichlet boundary conditions $\phi(\mathbf{X}) = 0$ along the origin and $\phi(\mathbf{X}) = 1$ along the terminus. To prevent fibers from passing through a part of the subdomain boundary, we impose homogeneous Neumann boundary conditions, $\partial\phi(\mathbf{X})/\partial\mathbf{N} = 0$, in which $\mathbf{N} = \mathbf{N}(\mathbf{X})$ is the unit normal to the subdomain boundary.

The ventricular material axes follow the rule-based method of Rossi et al.,¹⁹ which reflects experimentally characterized relationships between fiber angle and transmural position within the ventricular myocardium.^{21,25,26} In this approach, the sheet axis \mathbf{e}_s is generated first by the harmonic interpolation procedure with boundary conditions $\phi(\mathbf{X}) = 0$ on the endocardium and $\phi(\mathbf{X}) = 1$ on the epicardium, which produces a transmurally oriented direction field. A reference direction field that runs from the heart's apex to the mitral and tricuspid annuli through the ventricular myocardium is generated in each ventricle as $\mathbf{e}_{n_0} = \mathbf{c} - (\mathbf{c} \cdot \mathbf{s}_0)\mathbf{s}_0$, in which \mathbf{c} is the vector pointing from the apex to the center of the chamber's atrioventricular valve ring. An initial circumferential field is then created by setting $\mathbf{e}_{f_0} = \mathbf{e}_s \times \mathbf{e}_{n_0}$. Next, \mathbf{e}_{f_0} is rotated about the \mathbf{e}_s axis to capture transmural fiber rotation according to rules^{19,32} based on histology studies of the ventricular myocardium^{21,25,26} to generate the myofiber orientation \mathbf{e}_f . Finally, we set $\mathbf{e}_n = \mathbf{e}_f \times \mathbf{e}_s$.

The myofiber architecture of the atria is substantially more complex than the ventricular fiber structure, but prior studies have identified subregions within the atria with distinct principal myofiber orientations that are amenable to rule-based fiber models.^{24,59,60} Herein we use a version of the rule-based approach detailed by Rossi et al.²⁰ As with the ventricles, a transmural direction field \mathbf{e}_s is generated by setting the boundary conditions $\phi(\mathbf{X}) = 0$ on the endocardial surface and $\phi(\mathbf{X}) = 1$ on the epicardial surface. The atria are then partitioned into anatomical subregions. Within each subregion, the principal myofiber orientation is known, and subdomain boundary conditions are applied to generate the required myofiber field \mathbf{e}_f . Finally, we set $\mathbf{e}_n = \mathbf{e}_f \times \mathbf{e}_s$, as in the ventricles.

The method for generating the collagen fiber network in the valves is adopted from Hasan et al.¹⁸ The transmural direction field \mathbf{e}_n is generated by setting $\phi(\mathbf{X}) = 0$ on the leaflet surface facing the ventricle and $\phi(\mathbf{X}) = 1$ on the leaflet surface facing the great vessels and the atria for the semilunar valves and atrioventricular valves, respectively. A radial direction field, \mathbf{e}_s , is generated in each leaflet by setting $\phi(\mathbf{X}) = 0$ on the edge where the leaflet intersects with the myocardium and $\phi(\mathbf{X}) = 1$ along the leaflet's free edge. The circumferential direction field corresponding to

the mean collagen fiber axis is then determined as $\mathbf{e}_f = \mathbf{e}_s \times \mathbf{e}_n$. The chordae tendineae fiber axes \mathbf{e}_f are captured by setting $\phi(\mathbf{X}) = 0$ on the surfaces where the chordae meet the papillary muscles and $\phi(\mathbf{X}) = 1$ on the surfaces where the chordae meet the valve leaflets.

Material characterization

The biomechanical responses of all major structures of the heart are described using the framework of large deformation elasticity. Briefly, Ω_0^s is a Lagrangian reference coordinate system attached to the initial configuration of the heart, and Ω_t^s is the current configuration at time t . The deformation mapping $\chi : (\Omega_0^s, t) \mapsto \Omega_t^s$ relates reference and current coordinates, so that $\chi(\mathbf{X}, t) \in \Omega_t^s$ is the current position of $\mathbf{X} \in \Omega_0^s$ at time t . The mechanical responses of all structural components are defined by hyperelastic energy functionals \mathcal{W} of the deformation gradient tensor $\mathbb{F}(\mathbf{X}, t) = \partial\chi(\mathbf{X}, t)/\partial\mathbf{X}$.³² We describe myocardial contractile mechanics using an active strain approach,³³ which assumes that the Helmholtz free energy \mathcal{W} can be expressed using \mathbb{F} and an internal variable \mathbb{F}_A that represents the active component of the deformation, so that $\mathcal{W} = \mathcal{W}(\mathbb{F}, \mathbb{F}_A)$. The active strain model links \mathbb{F} and \mathbb{F}_A through an intermediate virtual configuration, so that $\mathbb{F} = \mathbb{F}_E \mathbb{F}_A$, and it assumes that the energy can be defined in the intermediate configuration, such that $\mathcal{W}(\mathbb{F}, \mathbb{F}_A) = \mathcal{W}(\mathbb{F}_E) = \mathcal{W}(\mathbb{F} \mathbb{F}_A^{-1})$.¹⁹

Different strain-energy functionals are used for different structures to reflect their specific material properties. Following the principle of material objectivity, the hyperelastic models are formulated using the right Cauchy-Green strain tensor, $\mathbb{C} = \mathbb{F}^T \mathbb{F}$, in terms of $I_1 = \text{tr}(\mathbb{C})$, $I_{4i} = \mathbf{e}_i^T \mathbb{C} \mathbf{e}_i$, $I_{4i}^* = \max(I_{4i}, 1)$, and $I_{8ij} = \mathbf{e}_i^T \mathbb{C} \mathbf{e}_j$, in which i and j index the material coordinate axes.

The ventricles and papillary muscles use the orthotropic Holzapfel-Ogden model,³²

$$\mathcal{W} = \frac{a}{2b} \exp(b(I_1 - 3)) + \sum_{i=f,s} \frac{a_i}{2b_i} (\exp(b_i(\kappa_i I_1 + (1 - 3\kappa_i)I_{4i} - 1)^2) - 1) + \frac{a_{fs}}{2b_{fs}} (\exp(b_{fs} I_{8fs}^2) - 1). \quad (1)$$

We use material parameters from Gültekin et al.¹⁴ that are based on triaxial shear tests on cuboid specimens of human left ventricles. The atria use the model of Augustin et al.,¹³

$$\mathcal{W} = \frac{a}{2b} (\exp(b(I_1 - 3)) - 1) + \frac{a_f}{2b_f} (\exp(b_f(\kappa I_1 + (1 - 3\kappa)I_{4f} - 1)^2) - 1). \quad (2)$$

We use material parameters from Augustin et al.¹³ that were calibrated using biaxial strain test data from anterior and posterior specimens of human left atria. The parameters κ_i in Eq. (1) and κ in Eq. (2) characterize myofiber angle dispersion.^{13,32}

The valve leaflets use a version of the Holzapfel-Gasser-Ogden model⁶¹ by Murdock et al.,⁶²

$$\mathcal{W} = a \{ \exp[b(I_1 - 3)] - 1 \} + \frac{a_f}{2b_f} \sum_{k \in \{+, -\}} \{ \exp[b_f (I_{4f}^* - 1)^2] - 1 \}. \quad (3)$$

We fit the parameters for all valves using biaxial stress-strain data generated by Pham et al.,¹⁶ as described below. Notice that the collagen fiber stresses in our leaflet models engage in tension but not in compression, which corresponds to the concept that collagen fibers collapse under compression and do not substantially contribute to the stress response of the material.⁶³ The chordae tendineae use a nonlinear spring model,

$$\mathcal{W} = \frac{a}{2} (I_1 - 3) + \frac{a_f}{3} (I_{4f}^* - 1)^3. \quad (4)$$

We determined mitral chordae parameters for the posterior and anterior leaflet chordae from uniaxial stress-strain tests of human mitral chordae,¹⁷ as described below. We also determined tricuspid chordae parameters from uniaxial stress-strain tests of human tricuspid chordae,¹⁵ all tricuspid chordae use the same parameters because of limited availability of human tissue data. Briefly, to determine material parameters, we extracted stress-strain curves using WebPlotDigitizer⁶⁴ and fit the constitutive model using `lsqcurvefit` in MATLAB (MathWorks, Natick, MA) with a tolerance of 1e-12. Fig. S6 shows our model fits.

Tissue	a [kPa]	b	a_f [kPa]	b_f	κ_f	θ_f [rad]	a_s [kPa]	b_s	κ_s	a_{fs} [kPa]	b_{fs}
Ventricles ¹⁴	0.4	6.55	3.05	29.05	0.08	-	1.25	36.65	0.09	0.15	6.28
Papillary Muscles ¹⁴	0.4	6.55	3.05	29.05	0.08	-	1.25	36.65	0.09	0.15	6.28
Atria ¹³	2.92	5.6	11.84	17.95	0.17	-	-	-	-	-	-
Aortic Valve ¹⁶	0.172	25.24	10.2	384.6	-	0.1055	-	-	-	-	-
Anterior Mitral Leaflet ¹⁶	0.398	14.91	11.1	104.9	-	0.7746	-	-	-	-	-
Posterior Mitral Leaflet ¹⁶	0.24	15.63	2.462	84.1	-	0.0	-	-	-	-	-
Pulmonary Valve ¹⁶	0.2135	11.14	0.9634	49.66	-	0.0001	-	-	-	-	-
Tricuspid Valve ¹⁶	0.1502	15.23	0.3157	40.73	-	0.0058	-	-	-	-	-
Anterior Mitral Basal Chordae ¹⁷	5.718e3	-	2.26e5	-	-	-	-	-	-	-	-
Anterior Mitral Marginal Chordae ¹⁷	1.619e4	-	1.679e5	-	-	-	-	-	-	-	-
Anterior Mitral Strut Chordae ¹⁷	1.0e3	-	2.652e5	-	-	-	-	-	-	-	-
Posterior Mitral Basal Chordae ¹⁷	4.796e3	-	1.904e5	-	-	-	-	-	-	-	-
Posterior Mitral Marginal Chordae ¹⁷	1.105e4	-	3.177e5	-	-	-	-	-	-	-	-
Tricuspid Valve Chordae ¹⁵	4.091e4	-	1.66e5	-	-	-	-	-	-	-	-
Aorta	1.2e2	-	-	-	-	-	-	-	-	-	-
Vena Cavae	1.43e2	-	-	-	-	-	-	-	-	-	-
Pulmonary Artery	1.0e2	-	-	-	-	-	-	-	-	-	-
Pulmonary Veins	1.43e2	-	-	-	-	-	-	-	-	-	-

Table 2: The numerical bulk modulus $\beta_s = 4.0e4$ kPa throughout the entire structure. Citations are included for the origin of the data that were used for the parameter fitting or the parameters themselves. As stated in the main text, the material parameters for the great vessels are used to prevent gross deformations and are not based on human tissue studies.

To avoid severe mitral valve regurgitation, we prestrained some chordae along their major fiber axes. This was necessary because the model construction process produced some loose chordae, which led to valve prolapse during ventricular systole. We used a prestraining approach that is equivalent to the active strain formulation for the myocardium,³³ but with fiber stretch γ_f constant in time. The fiber stretch terms for the eighteen mitral valve chordae range in values from 0.0 to 0.25, with the majority set to 0.15.

The vena cavae, pulmonary veins, ascending aorta, and pulmonary artery are modeled as neo-Hookean materials,

$$\mathcal{W} = \frac{a}{2}(I_1 - 3). \quad (5)$$

Model parameters were chosen to allow for realistic vessel compliance while avoiding excessive deformation across the cardiac cycle.

Table 2 lists all constitutive model parameters.

Active contraction

In the active strain formulation, \mathbb{F}_A defines the time-dependent change in the reference configuration resulting from muscle contraction.³³ We use

$$\mathbb{F}_A = \mathbb{1} + \gamma_f \mathbf{e}_f \otimes \mathbf{e}_f + \gamma_s \mathbf{e}_s \otimes \mathbf{e}_s + \gamma_n \mathbf{e}_n \otimes \mathbf{e}_n, \quad (6)$$

in which γ_i defines the deformation scaling along each material axis $i \in \{f, s, n\}$. The contraction of the myocardium is assumed to be volume-preserving, so $\det(\mathbb{F}_A) = 1$, and, for simplicity, transversely isotropic along the fiber axis \mathbf{e}_f . We prescribe $\gamma_f(t)$ and thereby obtain $\gamma_n(t) = \gamma_s(t) = (1 + \gamma_f(t))^{-1/2} - 1$.

Chamber	t_{delay} (s)	t_{peak} (s)	t_{plateau} (s)	t_{drop} (s)	$\gamma_{f,\text{max}}$
Atria	0.0	0.2	0.01	0.25	0.08
Ventricles	0.18 ⁶⁵	0.45	0.01	0.3	0.27

Table 3: Parameters for the active strain approach in the myocardium. The contraction period is 1 second.

The contraction timings for the atria and ventricles are based on studies of conduction propagation through the atria, atrioventricular node, and ventricles,⁶⁵ as well as pressure profiles measured within the chambers.⁴³ We defined the activation waveform by the function

$$g(t) = \begin{cases} \frac{1}{2} - \frac{1}{2} \cos\left(\frac{\pi}{t_{\text{peak}}} t\right) & \text{if } t - t_{\text{delay}} < t_{\text{delay}}, \\ 1 & \text{if } t_{\text{peak}} \leq t - t_{\text{delay}} \leq t_{\text{plateau}} + t_{\text{peak}}, \\ \frac{1}{2} + \frac{1}{2} \cos\left(\frac{\pi}{t_{\text{drop}}}(t - t_{\text{peak}} - t_{\text{plateau}})\right) & \text{if } t_{\text{plateau}} + t_{\text{peak}} < t - t_{\text{delay}} < t_{\text{plateau}} + t_{\text{peak}} + t_{\text{drop}}, \end{cases} \quad (7)$$

in which t_{delay} is the time from the beginning of the cycle to the start of contraction, t_{peak} is the time to peak contraction after the onset of contraction, t_{plateau} is the time spent at peak contraction, and t_{drop} is the time from the end of peak contraction to no contraction. Together with the magnitude of peak contraction, $\gamma_{f,\text{max}}$, we have $\gamma_f(t) = \gamma_{f,\text{max}} g(t)$. The active strain parameters for the atria and the ventricles are stated in Table 3, and the respective waveforms are visualized in the bottom right panel of Fig. 2. The majority of the parameters were acquired through manual calibration except for the ventricular t_{delay} , which was chosen to correspond to the time it takes for the activation signal to propagate from the sinoatrial node to the ventricles.⁶⁵

Pericardium

Following the approach of Pfaller et al.,³⁵ the force from the pericardium, $\mathbf{F}(\mathbf{X}, t)$, imposed on the epicardial surface, is determined by a system of distributed damped springs via

$$\mathbf{F}(\mathbf{X}, t) = \mathbf{n}(\mathbf{X}, t) \otimes \mathbf{n}(\mathbf{X}, t) [\kappa (\mathbf{X} - \chi(\mathbf{X}, t)) - \eta \mathbf{U}(\mathbf{X}, t)], \quad (8)$$

in which $\mathbf{n}(\mathbf{X}, t)$ is the surface unit normal to the epicardium in the current configuration, $\mathbf{U}(\mathbf{X}, t)$ is the velocity in the current configuration of material point \mathbf{X} , κ is a tethering constant, and η is a damping constant. Fig. 1(b) shows a schematic of the pericardium model superimposed with the full heart geometry. In our simulations, the parameters for the pericardium model are $\kappa = 1.0$ kPa/mm and $\eta = 5.0\text{e-}2$ kPa·s/mm. These parameters were chosen to limit gross epicardial oscillations, especially during ventricular relaxation.

Blood and Circulation

At the length scale of the heart, blood behaves like a Newtonian fluid,⁷ and the dynamics of blood are well approximated by the incompressible Navier-Stokes equations. We choose uniform mass density $\rho = 1.0$ g·cm⁻³ and uniform dynamic viscosity $\mu = 4$ mPa·s.⁶⁶

The afterload provided by the systemic and pulmonary circulations are described using three-element Windkessel models applied at locations where the ascending aorta (Ao) and the left and right pulmonary artery branches (LPA and RPA) intersect the boundary of the computational domain.³⁶ The state variable for each of these models is the afterload pressure, downstream of the great vessel, that satisfies the equation

$$C_i \frac{dp_{wk,i}}{dt} + R_{p,i} p_{wk,i} = Q_{outflow,i}, \quad i \in \{\text{Ao, LPA, RPA}\}. \quad (9)$$

$Q_{outflow,i}$ is the volume of blood per unit time leaving vessel i at the boundary of the computational domain. The Windkessel parameters for the great vessels were calibrated by querying the outflow rate waveforms and adjusting the peripheral resistance and compliance terms to maintain physiologic pressures at the boundary⁴³ following a procedure described below. The models of the peripheral circulations used in this study are not closed, and flows and pressures from the left and right sides of the heart are uncoupled. Instead, venous return is modeled by a pressure-driven flow source located in each atrium (LA and RA).³⁷ The flow sources are determined by

$$L_j \frac{dQ_j}{dt} + R_j Q_j = p_{source,j} - p_{atrium,j}, \quad j \in \{\text{LA, RA}\}, \quad (10)$$

in which $p_{source,j}$ is the pressure upstream of the respective atrium, which is treated as constant, and $p_{atrium,j}$ is the pressure sampled within the chamber. The ratio of the parameters L_j and R_j governs the timescale of the flow to the difference between the source and atrium pressures. Fig. 1(b) shows the Windkessel circulation models and the flow sources in relation to the full heart geometry.

Vessel	R_C (mmHg·s/mL)	R_p (mmHg·s/mL)	C (mL/mmHg)
Aorta	0.033 ³⁶	1.46	0.7
Pulmonary Arteries	0.0219	0.08	5.56

Table 4: The systemic circulation Windkessel parameters are tuned to the flow rate output at the edge of the ascending aorta. The pulmonary circulation Windkessel parameters are based on in vivo pressure measurements.

Parameters for the aorta and the pulmonary arteries are provided in Table 4. The characteristic resistance value for the aorta was taken from Sturgiopoulos et al.³⁶ The peripheral resistance and compliance were calibrated to fit specific flows generated from contraction of the left ventricle. The first step of this calibration procedure was to calculate the flow rate waveform at the intersection of the aorta with the edge of the computational domain; see Fig. S7(a). The parameters were then adjusted to generate physiologic systolic and diastolic pressure values.⁴³ Fig. S7(b) shows the Windkessel model predictions of the pressure waveform in the aorta as well as the pressure waveform downstream from the characteristic resistance. The model fit was tested, as illustrated in Fig. S7(c), by comparing the predicted pressure from the Windkessel model and the observed pressure at the intersection of the aorta and the computational domain. Over successive cycles, the pressure range generated by the model converges to the pressure wave predicted

by the specified Windkessel model parameters. This procedure mimics the baroreceptor reflex, which is a physiological control mechanism that adjusts vascular tone to maintain physiological blood pressure.³⁸

Parameters for the pulmonary arteries were based on pulmonary circulation values. To calculate nominal values for these parameters, we assumed a cardiac output of 100 mL/s. With the heart rate defined to be 60 BPM, the stroke volume is 100 mL. The pulmonary arteries were assumed to have a systolic pressure of 19 mmHg and diastolic pressure of 10 mmHg, with a mean pulmonary arterial pressure of 13 mmHg and a mean pulmonary venous pressure of 9 mmHg.⁶⁷ We assumed the mean pressure drop from the pulmonary arteries to the pulmonary veins is completely described by the peripheral resistance, and that the flow rate was equally split between the two pulmonary arteries. This resulted in a nominal value for the peripheral resistance of $R_p = 0.08$ mmHg·s/mL. The compliance value was calculated as the fraction of the stroke volume entering the artery divided by the pulse pressure. This resulted in a compliance value of 5.56 mL/mmHg. The pulmonary characteristic resistance was chosen to be of comparable magnitude to but smaller than the aortic characteristic resistance.

The flow source parameters were also determined empirically. The inertance of each source, which we have found to be most important with regards to maintaining numerical stability, is chosen to be time-step size dependent, and it is set to be as small as possible while preventing spurious changes in flow rate.³⁷ The resistances for both the left and right atrial sources are 0.15 mmHg·s/mL. For the right atrial source, the inertance is $300 \cdot \Delta t$ mmHg·s²/mL and the pressure source is 3.75 mmHg, where Δt is the time step size. For the left atrial source, the inertance is $240 \cdot \Delta t$ mmHg·s²/mL and the pressure source is 10 mmHg.

Fluid-Structure Interaction

Our model uses an immersed approach to simulating fluid-structure interaction (FSI). The immersed boundary (IB) method,⁹ introduced by Peskin to model the fluid dynamics of heart valves,⁶⁸ is the earliest example of such a numerical method. It treats fluid-structure systems in which an elastic structure is immersed in a viscous incompressible fluid. The IB method describes the structure in Lagrangian form and the fluid in Eulerian form, and it uses integral equations with Dirac delta function kernels to connect the Lagrangian and Eulerian frames. When the governing equations are discretized for computer simulation, the singular delta function is replaced by a regularized version of the delta function. Our computations use an efficient nodal version²⁹ of a stabilized immersed finite element-finite difference (IFED) method.²⁷ This scheme is a variation on the IB method that uses a finite element description of the structure, enabling structural models with complex geometries and realistic constitutive models. The IFED method also uses a regularized version of the Dirac delta function, and the choice of delta function used in this study follows results from a recent benchmarking study.⁶⁹ The remainder of this section outlines the IFED method and provides details on numerical discretization parameters used to generate simulation results.

Briefly, the IFED method predicts the coupled dynamics of the fluid-structure system within a computational domain Ω that is partitioned into non-overlapping fluid and solid subdomains, Ω_t^f and Ω_t^s , that are indexed by time t . To enable the use of fast structured-grid solvers, we require that $\Omega = \Omega_t^f \cup \Omega_t^s$ is a fixed rectangular region. Our simulations use a computational domain of size 20 cm×20 cm×20 cm, which is slightly larger than the bounding box that contains the reconstructed anatomy. The IFED formulation uses both Eulerian variables, which are described using fixed physical coordinates $\mathbf{x} \in \Omega$, and Lagrangian variables, which are described using material coordinates \mathbf{X} that are chosen to be the initial coordinates of the structure at time $t = 0$, so that $\mathbf{X} \in \Omega_0^s$. The deformation mapping $\chi : (\Omega_0^s, t) \mapsto \Omega_t^s \subseteq \Omega$ connects reference and current coordinates, so that $\chi(\mathbf{X}, t) \in \Omega_t^s$ is the current position of material point \mathbf{X} at time t .

The equations of motion for the coupled fluid-structure system are

$$\rho \left(\frac{\partial \mathbf{u}}{\partial t}(\mathbf{x}, t) + \mathbf{u}(\mathbf{x}, t) \cdot \nabla \mathbf{u}(\mathbf{x}, t) \right) = -\nabla p(\mathbf{x}, t) + \mu \nabla^2 \mathbf{u}(\mathbf{x}, t) + \mathbf{f}(\mathbf{x}, t), \quad \mathbf{x} \in \Omega, \quad (11)$$

$$\nabla \cdot \mathbf{u}(\mathbf{x}, t) = 0, \quad \mathbf{x} \in \Omega, \quad (12)$$

$$\mathbf{f}(\mathbf{x}, t) = \int_{\Omega_0^s} \mathbf{F}(\mathbf{X}, t) \delta(\mathbf{x} - \chi(\mathbf{X}, t)) d\mathbf{X}, \quad \mathbf{x} \in \Omega, \quad (13)$$

$$\frac{\partial \chi}{\partial t}(\mathbf{X}, t) = \mathbf{U}(\mathbf{X}, t) = \int_{\Omega} \mathbf{u}(\mathbf{x}, t) \delta(\mathbf{x} - \chi(\mathbf{X}, t)) d\mathbf{x}, \quad \mathbf{X} \in \Omega_0^s, \quad (14)$$

in which $\mathbf{u}(\mathbf{x}, t)$ and $\mathbf{U}(\mathbf{X}, t)$ are Eulerian and Lagrangian velocity fields, $p(\mathbf{x}, t)$ is the pressure, $\mathbf{f}(\mathbf{x}, t)$ and $\mathbf{F}(\mathbf{X}, t)$ are Eulerian and Lagrangian elastic force densities, ρ is the mass density of the fluid-structure system, μ is the viscosity, and $\delta(\mathbf{x})$ is the Dirac delta function. The Lagrangian elastic force density is defined in terms of the first Piola-Kirchhoff structural stress tensor, $\mathbb{P}(\mathbf{X}, t) = \frac{\partial \mathcal{W}}{\partial \mathbb{F}}(\mathbf{X}, t)$, by requiring $\mathbf{F}(\mathbf{X}, t)$ to satisfy

$$\int_{\Omega_0^s} \mathbf{F}(\mathbf{x}, t) \cdot \boldsymbol{\psi}(\mathbf{X}) d\mathbf{X} = - \int_{\Omega_0^s} \mathbb{P}(\mathbf{X}, t) : \nabla_{\mathbf{X}} \boldsymbol{\psi}(\mathbf{X}) d\mathbf{X} \quad (15)$$

for all smooth vector-valued test functions $\boldsymbol{\psi}(\mathbf{X})$. See Boffi et al.⁷⁰ and Griffith and Luo²⁷ for additional discussion.

As detailed in Methods Section *Cardiac Biomechanics Models*, the biomechanical response of the heart, its valves, and the nearby great vessels are described using hyperelastic constitutive models that are formulated using elastic energy functionals \mathcal{W} of invariants and pseudo-invariants of the right Cauchy-Green strain, $\mathbb{C} = \mathbb{F}^T \mathbb{F}$, in which $\mathbb{F} = \partial \chi / \partial \mathbf{X}$ is the deformation gradient tensor and $J = \det(\mathbb{F})$ is the Jacobian determinant. Although the continuum formulation of the IFED method generates exactly incompressible deformations, for which $J \equiv 1$, this property is generally lost when the continuous equations are discretized because of both spatial and temporal discretization effects. To mitigate these errors, we have found that it is beneficial to adopt a nearly incompressible material formulation.⁷¹ To do so, it is convenient to introduce the so-called modified Cauchy-Green strain, $\bar{\mathbb{C}} = \bar{\mathbb{F}}^T \bar{\mathbb{F}}$ with $\bar{\mathbb{F}} = J^{-\frac{1}{3}} \mathbb{F}$. Notice that $\det(\bar{\mathbb{F}}) = 1$, so $\bar{\mathbb{C}}$ encodes only deviatoric deformations but not dilatational motions. We denote by $\bar{\mathcal{W}}$ elastic energies that use invariants of $\bar{\mathbb{C}}$, i.e., in terms of the modified invariant $\bar{I}_1 = \text{tr}(\bar{\mathbb{C}})$ instead of $I_1 = \text{tr}(\mathbb{C})$. We do not use modified pseudo-invariants, because doing so can result in non-physical deformations.⁷² In addition, we introduce a volumetric energy,

$$\mathcal{U}(J) = \beta_s (J \log(J) - J + 1), \quad (16)$$

which penalizes changes in volume, in which β_s is the numerical bulk modulus.⁷¹ The bulk modulus, 4.0e4 kPa, is the same throughout the entire structure. We use $\bar{\mathcal{W}}$ and \mathcal{U} to evaluate the first Piola-Kirchhoff elastic stress via

$$\mathbb{P} = \frac{\partial \bar{\mathcal{W}}}{\partial \mathbb{F}} + \frac{\partial \mathcal{U}}{\partial \mathbb{F}}. \quad (17)$$

See Vadala-Roth et al.⁷¹ for further details.

In our simulations, we use an adaptive staggered-grid discretization of the incompressible Navier-Stokes equations detailed by Griffith⁷³ and a finite element description of Lagrangian equations describing the deformation the immersed structures and the resulting force generation.²⁷ The interaction equations, Eqs. (13) and (14), are discretized using an efficient nodal coupling scheme,²⁹ and we replace the singular delta function with a three-point B-spline kernel that was found to provide excellent accuracy and robustness compared to other commonly used choices.⁶⁹ The locally refined Cartesian grid is comprised of two nested grid levels with a refinement ratio of four between levels, and it provides a fine-grid spatial resolution of 0.43 mm. We use second-order centered differences for the Eulerian divergence, gradient, and Laplace operators along with a high-resolution upwind scheme for the convective terms.⁷³ We use standard P^2 (quadratic) tetrahedral elements to describe the structure. The Eulerian and Lagrangian variables are coupled using an explicit midpoint method,⁷³ and the incompressible Navier-Stokes equations are discretized in time using a semi-implicit scheme that uses the Crank-Nicolson method for the viscous terms and the second-order Adams-Bashforth scheme for the convective terms. We use a time-step size of 2.69 μs , which was chosen to be as large as possible while avoiding volumetric instability in the structure.

Flow Rate, Chamber Volume, and Pressure

We identify valve annuli upstream of each of the four heart valves, and we construct surface meshes where blood velocities are sampled to evaluate volumetric flow rates through each valve. The flow rate is captured every 100 time

steps. Flow volumes associated with each valve are obtained by integrating the flow rate via the trapezoidal rule. After the volume changes are computed, the flow rate data and volume contributions are down sampled to every 0.01 s for plotting output. The volume that passes through the aortic valve and mitral valve is used in conjunction with the initial volume of the ventricle to compute the evolving left ventricular volume. The initial volume of the left ventricle was estimated by extracting a surface mesh of the left ventricular endocardium that was then capped by the mitral and aortic valve annular meshes. The mesh manipulation and volume computation was done using Meshmixer (Autodesk, San Rafael, CA). The left ventricular pressure is approximated by querying the pressure at the centroid of the left ventricular endocardial surface at every time step. Pressure data are down sampled to every 0.01 s and smoothed using a three point moving average by the smooth function in MATLAB (MathWorks, Natick, MA).

Data Availability

All data supporting the conclusions of this study are included in the manuscript and supporting information.

Code Availability

The model was built using the IBAMR software infrastructure available on GitHub (ibamr.github.io), which is released under a permissive open-source license. This software relies on SAMRAI⁷⁴ for its finite difference framework, libMesh⁷⁵ for its finite element framework, and PETSc^{76–78} for its linear solver infrastructure.

References

- ¹ Clayton M (2012) Medicine: Leonardo's anatomy years. *Nature* 484(7394):314–316.
- ² Radisic M, et al. (2004) Functional assembly of engineered myocardium by electrical stimulation of cardiac myocytes cultured on scaffolds. *Proc Natl Acad Sci U S A* 101(52):18129–18134.
- ³ Savadjiev P, et al. (2012) Heart wall myofibers are arranged in minimal surfaces to optimize organ function. *Proc Natl Acad Sci U S A* 109(24):9248–9253.
- ⁴ Ericsson AC, Crim MJ, Franklin CL (2013) A brief history of animal modeling. *Mo Med* 110(3):201–205.
- ⁵ Camacho P, Fan H, Liu Z, He JQ (2016) Large mammalian animal models of heart disease. *J Cardiovasc Dev and Dis* 3(4):30.
- ⁶ Morrison TM, Stitzel JD, Levine SM (2023) Modeling and simulation in biomedical engineering: Regulatory science and innovation for advancing public health. *Ann of Biomed Eng* 51(1):1–5.
- ⁷ Peskin CS, McQueen DM (1996) Fluid dynamics of the heart and its valves in *Case Studies in Mathematical Modeling: Ecology, Physiology, and Cell Biology*, eds. Othmer HG, Adler FR, Lewis MA, Dallon JC. (Prentice-Hall, Englewood Cliffs, NJ, USA), pp. 309–337.
- ⁸ McQueen DM, Peskin CS (2000) A three-dimensional computer model of the human heart for studying cardiac fluid dynamics. *Comput Graph (ACM)* 34(1):56–60.
- ⁹ Peskin CS (2002) The immersed boundary method. *Acta Numer* 11:479–517.
- ¹⁰ Baillargeon B, Rebelo N, Fox DD, Taylor RL, Kuhl E (2014) The Living Heart Project: A robust and integrative simulator for human heart function. *Eur J Mech A Solids* 48:38–47.
- ¹¹ Fedele M, et al. (2023) A comprehensive and biophysically detailed computational model of the whole human heart electromechanics. *Comput Methods Appl Mech Eng* 410:115983.

- ¹² Kariya T, et al. (2020) Personalized perioperative multi-scale, multi-physics heart simulation of double outlet right ventricle. *Ann Biomed Eng* 48(6):1740–1750.
- ¹³ Augustin CM, et al. (2019) The impact of wall thickness and curvature on wall stress in patient-specific electromechanical models of the left atrium. *Biomech Model Mechanobiol* 19(3):1015–1034.
- ¹⁴ Gültekin O, Sommer G, Holzapfel GA (2016) An orthotropic viscoelastic model for the passive myocardium: continuum basis and numerical treatment. *Comput Methods Biomech Biomed Engin* 19(15):1647–1664.
- ¹⁵ Lim KO (1980) Mechanical properties and ultrastructure of normal human tricuspid valve chordae tendineae. *Jpn J Physiol* 30(3):455–464.
- ¹⁶ Pham T, Sulejmani F, Shin E, Wang D, Sun W (2017) Quantification and comparison of the mechanical properties of four human cardiac valves. *Acta Biomater* 54:345–355.
- ¹⁷ Zuo K, et al. (2016) Characterization of biomechanical properties of aged human and ovine mitral valve chordae tendineae. *J Mechan Behav Biomed Mater* 62:607–618.
- ¹⁸ Hasan A, et al. (2017) Image-based immersed boundary model of the aortic root. *Med Eng Phys* 47:72–84.
- ¹⁹ Rossi S, Lassila T, Ruiz-Baier R, Sequeira A, Quarteroni A (2014) Thermodynamically consistent orthotropic activation model capturing ventricular systolic wall thickening in cardiac electromechanics. *Eur J Mech A Solids* 48(1):129–142.
- ²⁰ Rossi S, et al. (2022) Rule-based definition of muscle bundles in patient-specific models of the left atrium. *Front Physiol* 13:912947.
- ²¹ Arts T, Costa KD, Covell JW, McCulloch AD (2001) Relating myocardial laminar architecture to shear strain and muscle fiber orientation. *Am J Physiol Heart Circ Physiol* 280(5):H2222–H2229.
- ²² Bigi A, et al. (1982) Structure and orientation of collagen fibres in human mitral valve. *Int J Biol Macromol* 4(7):387–392.
- ²³ Driessen NJ, Bouten CV, Baaijens FP (2005) A structural constitutive model for collagenous cardiovascular tissues incorporating the angular fiber distribution. *J Biomech Eng* 127(3):494–503.
- ²⁴ Ho SY, Cabrera JA, Sánchez-Quintana D (2012) Left atrial anatomy revisited. *Circ Arrhythm Electrophysiol* 5(1):220–228.
- ²⁵ Nielsen PM, Le Grice IJ, Smaill BH, Hunter PJ (1991) Mathematical model of geometry and fibrous structure of the heart. *Am J Physiol* 260(4):H1365–H1378.
- ²⁶ Streeter DD, Hanna WT (1973) Engineering mechanics for successive states in canine left ventricular myocardium. II. Fiber angle and sarcomere length. *Circ Res* 33(6):656–664.
- ²⁷ Griffith BE, Luo X (2017) Hybrid finite difference/finite element immersed boundary method. *Int J Numer Method Biomed Eng* 33(12):e2888.
- ²⁸ Hu Y, Schneider T, Wang B, Zorin D, Panozzo D (2020) Fast tetrahedral meshing in the wild. *ACM Trans Graph* 39(4):117:1–117:18.
- ²⁹ Wells D, Vadala-Roth B, Lee JH, Griffith BE (2023) A nodal immersed finite element-finite difference method. *J Comput Phys* 477:111890.
- ³⁰ Palit A, et al. (2017) Passive diastolic modelling of human ventricles: effects of base movement and geometrical heterogeneity. *J Biomech* 52:95–105.

- ³¹ Di Carli MF, Geva T, Davidoff R (2016) The future of cardiovascular imaging. *Circulation* 133(25):2640–2661.
- ³² Holzapfel GA, Ogden RW (2009) Constitutive modelling of passive myocardium: a structurally based framework for material characterization. *Philos Trans A Math Phys Eng Sci* 367(1902):3445–3475.
- ³³ Ambrosi D, Pezzuto S (2012) Active stress vs. active strain in mechanobiology: Constitutive issues. *J Elast* 107(2):199–212.
- ³⁴ Klotz S, et al. (2006) Single-beat estimation of end-diastolic pressure-volume relationship: a novel method with potential for noninvasive application. *Am J Physiol Heart Circ Physiol* 291(1):H403–H412.
- ³⁵ Pfaller MR, et al. (2019) The importance of the pericardium for cardiac biomechanics: from physiology to computational modeling. *Biomech Model Mechanobiol* 18(2):503–529.
- ³⁶ Stergiopoulos N, Westerhof BE, Westerhof N (1999) Total arterial inertance as the fourth element of the windkessel model. *Am J Physiol* 276(1):H81–H88.
- ³⁷ Griffith BE (2005) Ph.D. thesis (New York University).
- ³⁸ Hall JE (2016) *Guyton and Hall Textbook of Medical Physiology*. (Elsevier, Philadelphia), Thirteenth edition.
- ³⁹ Cattermole GN, et al. (2017) The normal ranges of cardiovascular parameters measured using the ultrasonic cardiac output monitor. *Physiol Rep* 5(6):e13195.
- ⁴⁰ Watanabe H, Sugiura S, Kafuku H, Hisada T (2004) Multiphysics simulation of left ventricular filling dynamics using fluid-structure interaction finite element method. *Biophys J* 87(3):2074–2085.
- ⁴¹ Bastos MB, et al. (2020) Invasive left ventricle pressure-volume analysis: overview and practical clinical implications. *Eur Heart J* 41(12):1286–1297.
- ⁴² Patterson T, et al. (2021) Physiological impact of afterload reduction on cardiac mechanics and coronary hemodynamics following isosorbide dinitrate administration in ischemic heart disease. *J Cardiovasc Transl Res* 14(5):962–974.
- ⁴³ Murgu JP, Westerhof N, Giolma JP, Altobelli SA (1980) Aortic input impedance in normal man: relationship to pressure wave forms. *Circulation* 62(1):105–116.
- ⁴⁴ Mottram PM, Marwick TH (2005) Assessment of diastolic function: what the general cardiologist needs to know. *Heart* 91(5):681–695.
- ⁴⁵ Yellin EL, Nikolic S, Frater RW (1990) Left ventricular filling dynamics and diastolic function. *Prog Cardiovasc Dis* 32(4):247–271.
- ⁴⁶ Coffey S, et al. (2021) Global epidemiology of valvular heart disease. *Nat Rev Cardiol* 18(2):853–864.
- ⁴⁷ Segars WP, Mahesh M, Beck TJ, Frey EC, Tsui BM (2008) Realistic CT simulation using the 4D XCAT phantom. *Med Phys* 35(8):3800–3808.
- ⁴⁸ Segars WP, Sturgeon G, Mendonca S, Grimes J, Tsui BM (2010) 4D XCAT phantom for multimodality imaging research. *Med Phys* 37(9):4902–4915.
- ⁴⁹ Reul H, et al. (1990) The geometry of the aortic root in health, at valve disease and after valve replacement. *J Biomech* 23(2):181–191.
- ⁵⁰ Swanson WM, Clark RE (1974) Dimensions and geometric relationships of the human aortic valve as a function of pressure. *Circ Res* 35(6):871–882.

- ⁵¹ Clark RE, Finke EH (1974) Scanning and light microscopy of human aortic leaflets in stressed and relaxed states. *J Thorac Cardiovasc Surg* 67(5):792–804.
- ⁵² Khalighi AH, Drach A, Gorman RC, Gorman JH, Sacks MS (2018) Multi-resolution geometric modeling of the mitral heart valve leaflets. *Biomech Model Mechanobiol* 17(2):351–366.
- ⁵³ Lim KH, Yeo JH, Duran CM (2005) Three-dimensional asymmetrical modeling of the mitral valve: a finite element study with dynamic boundaries. *J Heart Valve Dis* 14(3):386–392.
- ⁵⁴ Prot V, Skallerud B (2009) Nonlinear solid finite element analysis of mitral valves with heterogeneous leaflet layers. *Comput Mech* 43:353–368.
- ⁵⁵ Lama P, Tamang BK, Kulkarni J (2016) Morphometry and aberrant morphology of the adult human tricuspid valve leaflets. *Anat Sci Int* 91(2):143–150.
- ⁵⁶ Skwarek M, Grzybiak M, Kosiński A, Hreczecha J (2004) Notes on the morphology of the tricuspid valve in the adult human heart. *Folia Morphol (Warsz)* 63(3):319–324.
- ⁵⁷ Khalighi AH, et al. (2019) Development of a functionally equivalent model of the mitral valve chordae tendinae through topology optimization. *Ann Biomed Eng* 47(1):60–74.
- ⁵⁸ Wong J, Kuhl E (2014) Generating fibre orientation maps in human heart models using Poisson interpolation. *Comput Methods Biomech Biomed Engin* 17(11):1217–1226.
- ⁵⁹ Ferrer A, et al. (2015) Detailed anatomical and electrophysiological models of human atria and torso for the simulation of atrial activation. *PLoS One* 10(11):e0141573.
- ⁶⁰ Krueger MW, et al. (2011) Modeling atrial fiber orientation in patient-specific geometries: A semi-automatic rule-based approach in *Functional Imaging and Modeling of the Heart*, eds. Metaxas D, Axel L. (Springer Berlin Heidelberg, Berlin, Heidelberg), pp. 223–232.
- ⁶¹ Holzapfel GA, Gasser TC, Ogden RW (2000) A new constitutive framework for arterial wall mechanics and a comparative study of material models. *J Elast* 61(1):1573–2681.
- ⁶² Murdock K, Martin C, Sun W (2018) Characterization of mechanical properties of pericardium tissue using planar biaxial tension and flexural deformation. *J Mech Behav Biomed Mater* 77:148–156.
- ⁶³ Gasser TC, Ogden RW, Holzapfel GA (2006) Hyperelastic modelling of arterial layers with distributed collagen fibre orientations. *J R Soc Interface* 3(6):15–35.
- ⁶⁴ Rohatgi A (2022) Webplotdigitizer: Version 4.6.
- ⁶⁵ Houthuizen P, Bracke FA, van Gelder BM (2011) Atrioventricular and interventricular delay optimization in cardiac resynchronization therapy: physiological principles and overview of available methods. *Heart Fail Rev* 16(3):263–276.
- ⁶⁶ Brindise MC, Busse MM, Vlachos PP (2018) Density and viscosity matched Newtonian and non-Newtonian blood-analog solutions with PDMS refractive index. *Exp Fluids* 59(11):173.
- ⁶⁷ Naeije R (2013) Physiology of the pulmonary circulation and the right heart. *Curr Hypertens Rep* 15(6):623–631.
- ⁶⁸ Peskin CS (1972) Flow patterns around heart valves: A numerical method. *J Comput Phys* 10(2):252–271.
- ⁶⁹ Lee JH, Griffith BE (2022) On the Lagrangian-Eulerian coupling in the immersed finite element/difference method. *J Comput Phys* 457:111042.

- ⁷⁰ Boffi D, Gastaldi L, Heltai L, Peskin CS (2008) On the hyper-elastic formulation of the immersed boundary method. *Comput Methods Appl Mech Eng* 197(25-28):2210–2231.
- ⁷¹ Vadala-Roth B, Acharya S, Patankar NA, Rossi S, Griffith BE (2020) Stabilization approaches for the hyperelastic immersed boundary method for problems of large-deformation incompressible elasticity. *Comput Methods Appl Mech Eng* 365:112978.
- ⁷² Sansour C (2008) On the physical assumptions underlying the volumetric-isochoric split and the case of anisotropy. *Front Physiol* 27(1):28–39.
- ⁷³ Griffith BE (2012) Immersed boundary model of aortic heart valve dynamics with physiological driving and loading conditions. *Int J Numer Method Biomed Eng* 28(3):317–345.
- ⁷⁴ Hornung RD, Kohn SR (2002) Managing application complexity in the SAMRAI object-oriented framework. *Concurr Comput* 14(5):347–368.
- ⁷⁵ Kirk BS, Peterson JW, Stogner RH, Carey GF (2006) libMesh: a c++ library for parallel adaptive mesh refinement/coarsening simulations. *Eng Comput* 22:237–254.
- ⁷⁶ Balay S, et al. (2022) PETSc Web page (<https://petsc.org/>).
- ⁷⁷ Balay S, et al. (2022) PETSc/TAO users manual, (Argonne National Laboratory), Technical Report ANL-21/39 - Revision 3.18.
- ⁷⁸ Balay S, Gropp WD, McInnes LC, Smith BF (1997) Efficient management of parallelism in object oriented numerical software libraries in *Modern Software Tools in Scientific Computing*, eds. Arge E, Bruaset A, Langtangen H. (Birkhäuser Press), pp. 163–202.

Acknowledgements

We acknowledge research funding from National Institutes of Health Awards R01HL117063, U01HL143336, and R01-HL157631 and National Science Foundation Awards DMS 1460368, OAC 1460334, OAC 1450327, OAC 1652541, and OAC 1931516. MD was supported in part by National Institutes of Health Institutional Training Grant Award T32-GM067553. CP was supported in part by National Science Foundation Research Training Group Award DMS 1646339. Computations were performed using facilities provided by the University of North Carolina at Chapel Hill through the Research Computing division of UNC Information Technology Services. BEG, CSP, and CP acknowledge discussions and contributions by David M. McQueen in the development of the immersed boundary method and its applications to predecessors of the model of cardiac fluid dynamics described in this study.

Author Contributions

Marshall Davey: Methodology; Software; Validation; Formal Analysis; Investigation; Data Curation; Writing - Original Draft; Writing - Review & Editing; Visualization. **Charles Puelz:** Conceptualization; Methodology; Software; Validation; Investigation; Writing - Original Draft; Writing - Review & Editing. **Simone Rossi:** Methodology; Software; Investigation; Writing - Review & Editing; Visualization. **Margaret Anne Smith:** Formal Analysis; Investigation; Data Curation. **David R. Wells:** Methodology; Software; Writing - Original Draft; Writing - Review & Editing. **Greg Sturgeon:** Methodology; Software; Formal Analysis; Investigation; Data Curation; Writing - Review & Editing. **Paul Segars:** Methodology; Software; Formal Analysis; Investigation; Data Curation; Resources; Writing - Review & Editing. **John P. Vavalle:** Validation; Writing - Review & Editing. **Charles S. Peskin:** Methodology; Validation; Writing - Review & Editing. **Boyce E. Griffith:** Conceptualization; Methodology; Software; Validation; Resources; Writing - Original Draft; Writing - Review & Editing; Supervision; Project Administration; Funding Acquisition. MD and CP contributed equally to this work. BEG is the corresponding author.

Competing Interests

The authors declare no competing interests.

Materials and Correspondence

Correspondence and material requests should be addressed to Boyce E. Griffith at boyceg@email.unc.edu.

SUPPLEMENTARY INFORMATION

Left Ventricular End-Diastolic Pressure-Volume Relationship

To provide a partial validation of the passive elastic response of the model heart, we generated the Klotz pressure-volume curve as detailed by Klotz et al.³⁴ To do so, we removed the pericardial tethering from the ventricular epicardium, applied loads of 5, 10, 15, 20, 25, and 30 mmHg to the endocardial surface of the left ventricle, and recorded the resulting chamber volume. The Klotz relation relies on a normalized volume $\tilde{v}(p)$ defined by

$$\tilde{v}(p) = \frac{v(p) - v_0}{v_{30} - v_0}, \quad (\text{S1})$$

in which $v(p)$ is the volume (mL) of the left ventricle at pressure p (mmHg), v_{30} is the volume of the left ventricle at 30 mmHg, and v_0 is the volume of the left ventricle at 0 mmHg. Fig. S2 shows the Klotz curve data generated by our model. We obtain good agreement to the reference curve, with a root mean squared error of 1.63 mmHg. This error is comparable to the root mean squared error of 2.99 ± 1.72 mmHg reported by Klotz et al. for in vivo human data.³⁴

Left Ventricular Volume Dynamics

Fig. S3 shows the time series data for the left ventricular volume that were used to generate the pressure-volume relation. The pressure data are shown in the main body of the text, but volume waveforms are much less commonly obtained in vivo. As mentioned in Methods Section *Flow Rate, Chamber Volume, and Pressure*, the left ventricular volume was estimated using the fluxes through the mitral and aortic valves along with an initial volume that was determined using numerical quadrature.

Clinical Pressure-Volume Relations

Fig. S4 compares the pressure-volume loops generated over successive cycles of the model to clinical pressure-volume relations.^{41,42} The mitral closing transients are apparent in the cusps in the bottom right corners of the clinical pressure-volume relations, though they are not as distinct as in the model. The closing transients for the aortic valve are not as clearly defined. The clinical pressure-volume relations also demonstrate that the transitions in and out of the isovolumetric phases are not sharp, and the isovolumetric phases are not strictly volume preserving, which is in clear contrast to the strict vertical phases seen in textbook pressure-volume loops.³⁸

Mitral Valve Performance

Fig. S5(a) compares digitized in vivo canine mitral flow rate data⁴⁵ to data generated by the model. In the first column, it is apparent that the mitral flow rate waveform shape generated by the model is qualitatively similar to the in vivo data, including the mitral valve closing transient indicated by the negative flow rate. For the model and in vivo flow rate waveforms, we compute the volume passing through the mitral valve over one cycle by integrating the flow rate data. The in vivo and model data look very similar in that there is a large increase in the volume output followed by a small loss in volume during the closing transient, more pronounced and prolonged in the model, and an eventual leveling of the volume. The right column plots the left-ventricular pressure against the volume passing through the mitral valve to show the contribution of the mitral valve flux to the total pressure-volume relationship. The in vivo pressure data come from the same source as the flow rate data, and the flow rate and pressure data were measured simultaneously.⁴⁵ The model and in vivo data show that the isovolumetric contraction periods are not truly isovolumetric because of the mitral valve closing transient and the method used to determine volume, which does not account for the dynamic fluid volume captured between the mitral valve ring and the closed mitral valve leaflets. These results are consistent with the clinical pressure-volume loops discussed in Section *Clinical Pressure-Volume Relations*.

Aortic Valve Performance

Fig. S5(b) compares digitized in vivo human aortic flow rate data⁴³ to data generated by the model. In the first column it is apparent that the aortic flow rate waveform shape generated by the model is qualitatively similar to the in vivo data, including the aortic valve closing transient indicated by the negative flow rate. For both cases, we compute the volume passing through the aortic valve over one cycle by integrating the flow rate waveform. The in vivo and model data look very similar in that there is a large increase in the volume output followed by a small loss in volume during the closing transient and a leveling of the volume, as seen in the second column. The right column plots the left-ventricular pressure against the volume passing through the aortic valve to show the contribution of the aortic valve flux to the total pressure-volume relationship, which shows clear volume gain during 'isovolumetric' relaxation for both the model and in vivo data. The in vivo pressure data comes from the same source as the flow rate data, and the flow rate and pressure data were measured simultaneously.⁴³

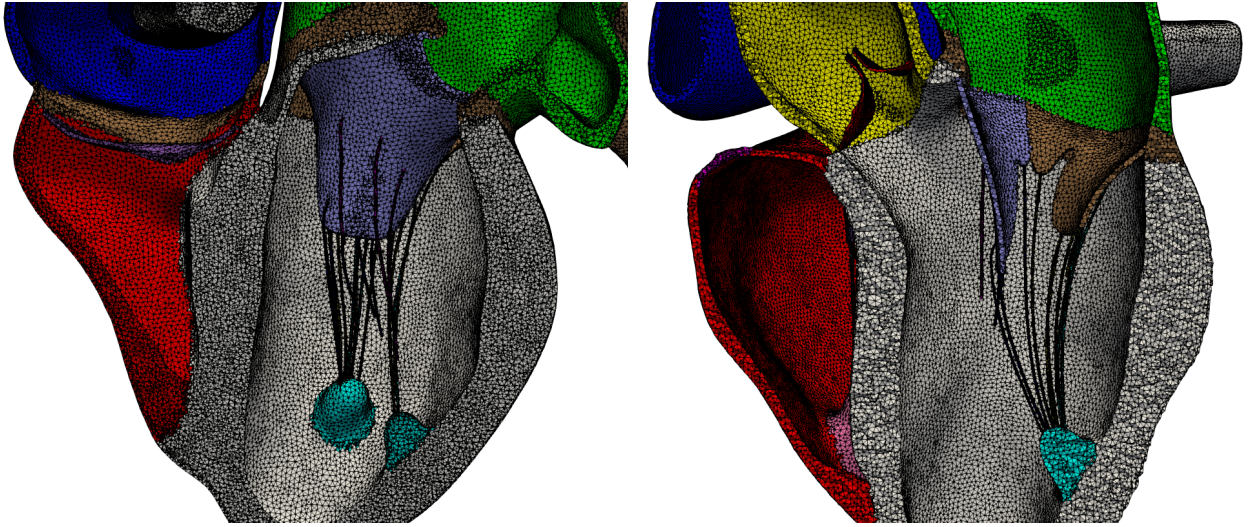


Figure S1: A visualization of the heart mesh with a focus on the left side and mitral valve apparatus. The mesh contains approximately 2.4 million tetrahedral elements with an average diameter of 1.17 mm. The colors denote different subdomains within the mesh.

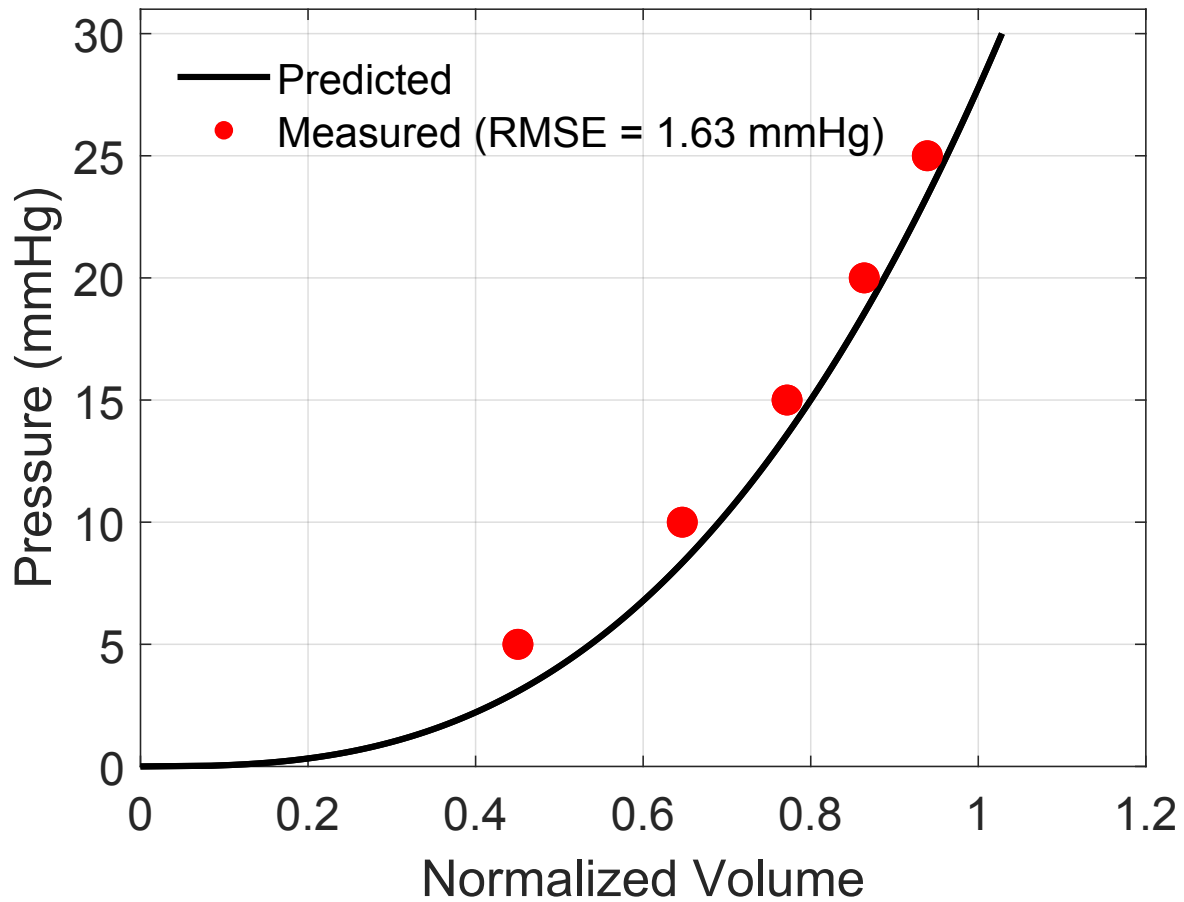


Figure S2: The Klotz curve generated from our model, which was used to verify the passive material parameters within the left ventricle.³⁴ Pressures of 5, 10, 15, 20, 25, and 30 mmHg were applied to the left ventricular endocardial surface with pericardial tethering removed from the epicardial surfaces. The resultant left ventricular volumes were 115.8, 124.3, 129.8, 133.8, 137.0, and 139.7 mL, respectively, with an initial left ventricular volume of 96.3 mL. Compared to the predicted curve estimated (black curve) by Klotz et al., the root mean squared error of the observed data (red dots) is 1.63 mmHg, which is well within to the observed in vivo human data range of 2.99 ± 1.72 mmHg.³⁴

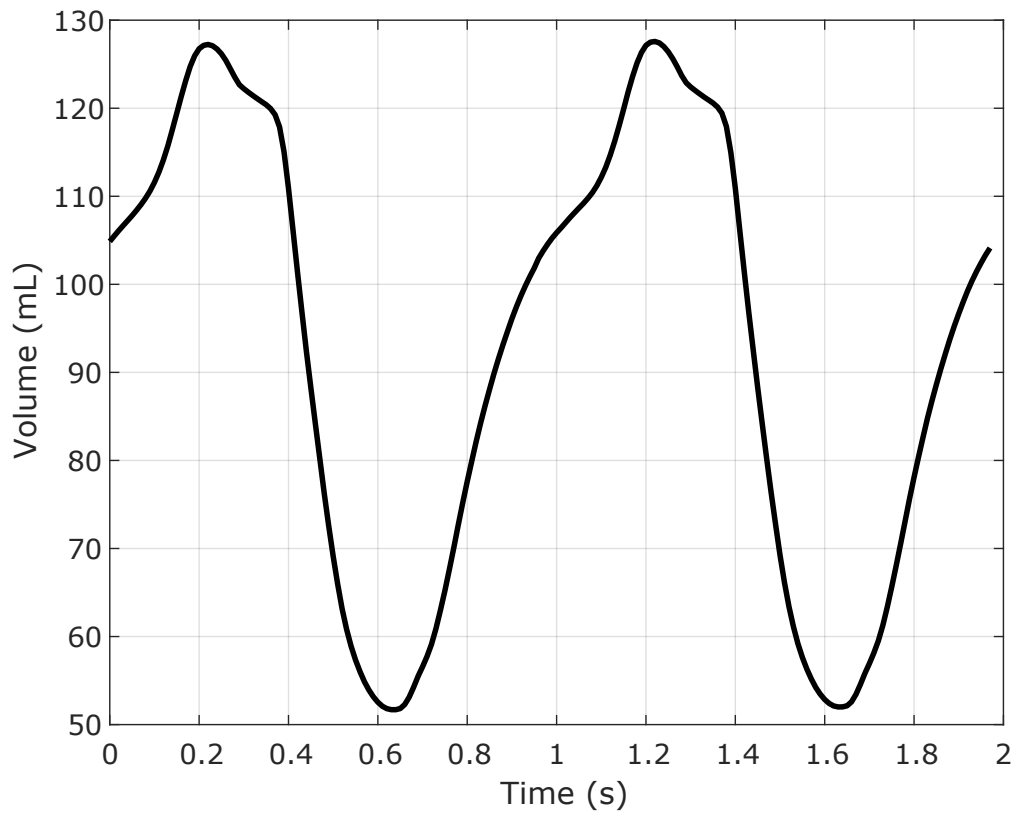


Figure S3: The total left ventricular volume during two successive cycles.

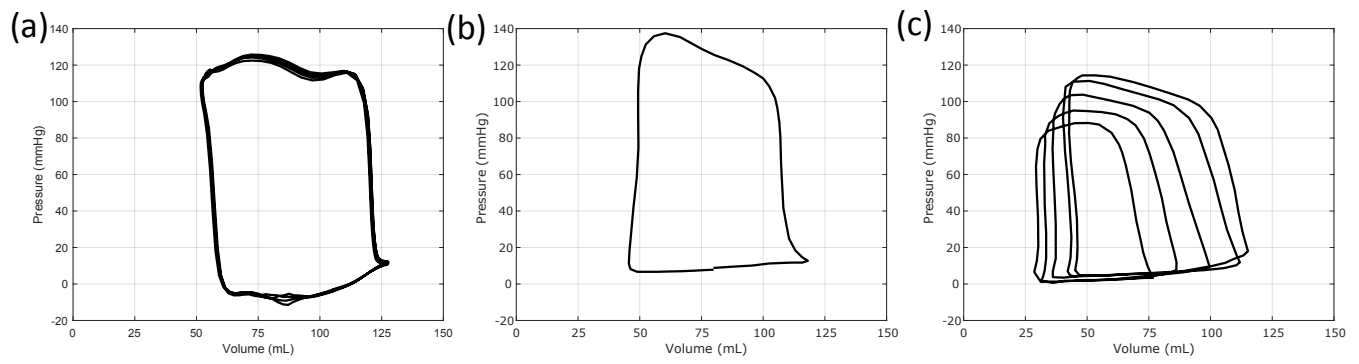


Figure S4: Successive pressure-volume curves from the fifth to eighth cycles of the model (a) compared to clinical pressure volume relations from a single cycle⁴² (b) and a Frank-Starling mechanism study via pulmonary vein occlusion⁴¹ (c).

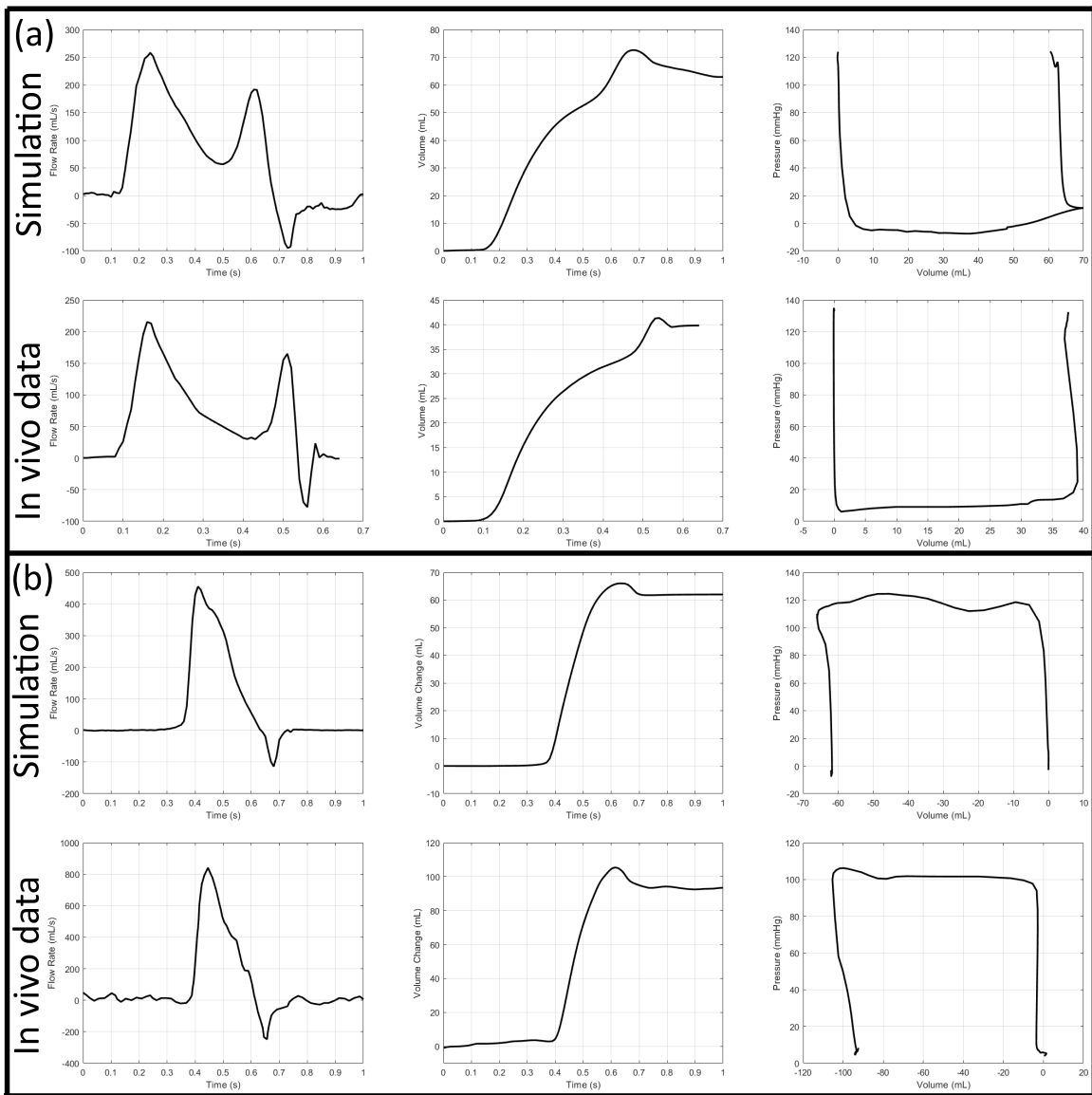


Figure S5: (a) Comparison of in vivo canine mitral valve flow rate data⁴⁵ to the model. The second column shows the volume that has passed through the mitral valve to the left ventricle during the cardiac cycle calculated by integrating the flow rate waveform. The third column shows the mitral valve contribution to the left ventricular pressure-volume relation. (b) Comparison of in vivo human aortic valve flow rate data⁴³ to the model. The second column shows the volume that has passed through the aortic valve into the aorta during the cardiac cycle calculated by integrating the flow rate waveform. The third column shows the aortic valve contribution to the left ventricular pressure-volume relation.

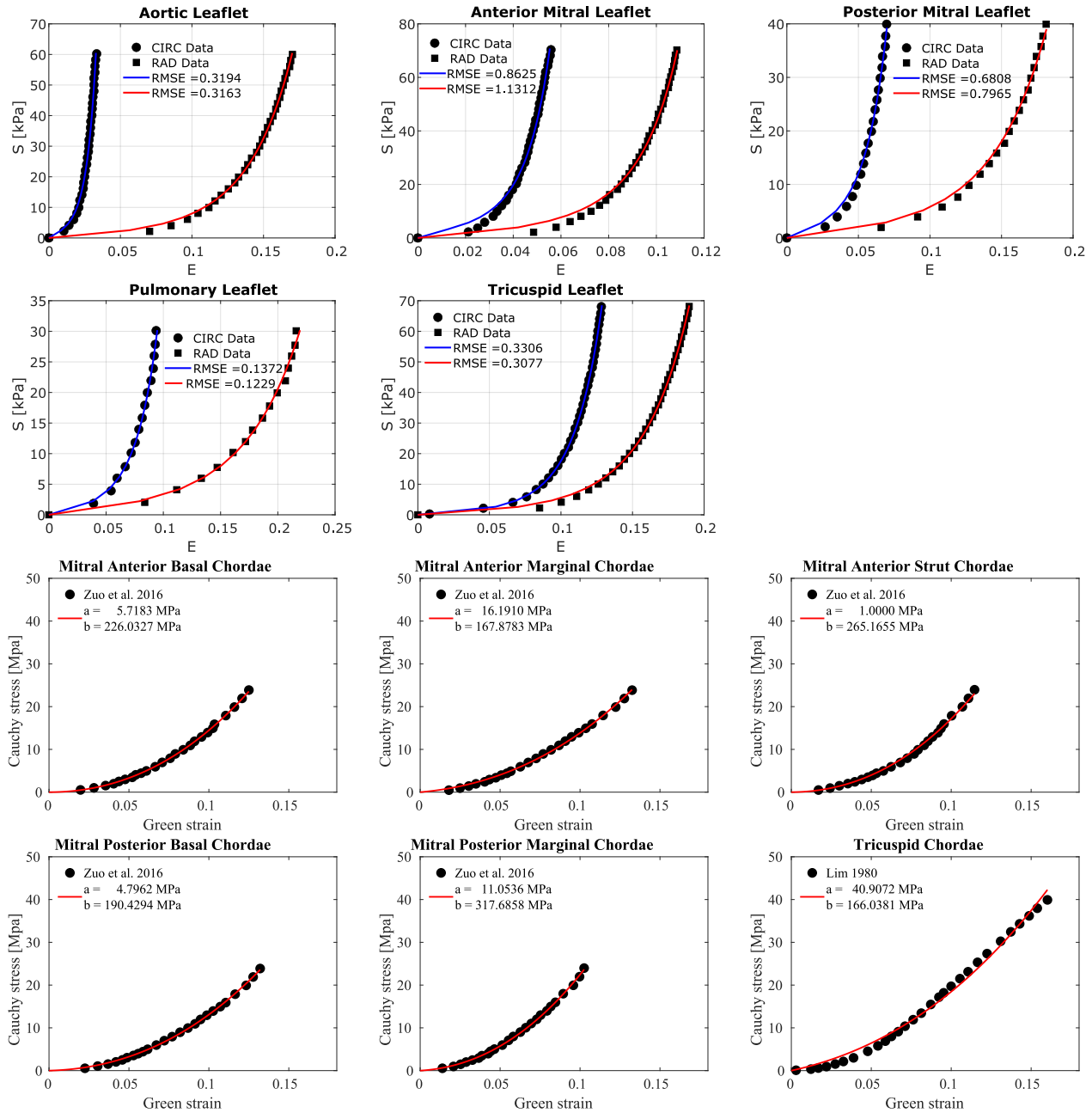


Figure S6: Parameters for the valve material models were derived from the results of biaxial stress-strain tests along the radial and circumferential directions executed by Pham et al.,¹⁶ and fit to a modified Holzapfel-Gasser-Ogden model proposed by Murdock et al.,⁶² Eq. (3). Data from mitral¹⁷ and tricuspid¹⁵ chordae stress-strain tests were fit to a generic nonlinear spring material model, Eq. (4). Digitized data are shown as the black circles and squares for circumferential and radial fiber directions, respectively, for the valves. The fits for the radial and circumferential data are shown as the red and blue lines, respectively, along with the corresponding root mean squared errors (RMSE) for the valve fits. The digitized data for the chordae are shown as black circles, and the fits are shown as the red curves with the resultant parameters listed.

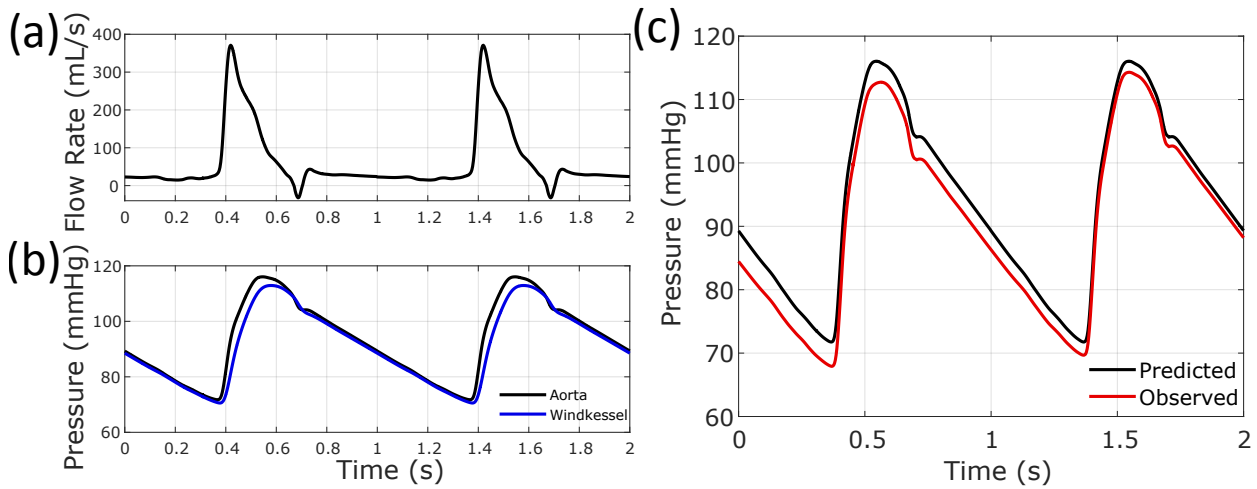


Figure S7: Workflow for tuning the Windkessel parameters for the aorta. (a) The tuning of the Windkessel parameters starts with extracting the flow rate waveforms from the top of the aorta. (b) The flow rate is then used to choose the compliance and peripheral resistance that lead to appropriate systolic and diastolic pressures in the aorta. (c) The model is then run with these parameters and the observed pressure values are validated against the predicted pressure waves. Over successive cycles, the observed pressure converges to the pressure wave predicted by the specified Windkessel model parameters.